UC Irvine
UC Irvine Previously Published Works

Title

Hierarchical Gradients of Encoded Spatial and Sensory Information in the Neocortex Are Attenuated by Dorsal Hippocampal Lesions.

Permalink

https://escholarship.org/uc/item/7xc0n259

Journal

The Journal of Neuroscience, 44(31)

Authors

Demchuk, Aubrey

Esteves, Ingrid

Chang, HaoRan

et al.

Publication Date

2024-07-31

DOI

10.1523/JNEUROSCI.1619-23.2024

Peer reviewed

Behavioral/Cognitive

Hierarchical Gradients of Encoded Spatial and Sensory Information in the Neocortex Are Attenuated by Dorsal Hippocampal Lesions

Aubrey M. Demchuk,[1] Ingrid M. Esteves,[1] HaoRan Chang,[1] Jianjun Sun,[2] and Bruce L. McNaughton[1,3]

[1]Canadian Centre for Behavioural Neuroscience, Department of Neuroscience, University of Lethbridge, Lethbridge, Alberta T1K 3M4, Canada, [2]Hotchkiss Brain Institute, University of Calgary Foothills, Calgary, Alberta T2N 4N1, Canada, and [3]Department of Neurobiology and Behaviour, University of California, Irvine, Irvine, California 92697

During navigation, the neocortex actively integrates learned spatial context with current sensory experience to guide behaviors. However, the relative encoding of spatial and sensorimotor information among cortical cells, and whether hippocampal feedback continues to modify these properties after learning, remains poorly understood. Thus, two-photon microscopy of male and female Thy1-GCaMP6s mice was used to longitudinally image neurons spanning superficial retrosplenial cortex and layers II–Va of primary and secondary motor cortices before and after bilateral dorsal hippocampal lesions. During behavior on a familiar cued treadmill, the locations of two obstacles were interchanged to decouple place-tuning from cue-tuning among position-correlated cells with fields at those locations. Subpopulations of place and cue cells each formed interareal gradients such that higher-level cortical regions exhibited higher fractions of place cells, whereas lower-level regions exhibited higher fractions of cue cells. Position-correlated cells in the motor cortex also formed translaminar gradients; more superficial cells were more likely to exhibit fields and were more sparsely and precisely tuned than deeper cells. After dorsal hippocampal lesions, a neural representation of the learned environment persisted, but retrosplenial cortex exhibited significantly increased cue-tuning, and, in motor cortices, both position-correlated cell recruitment and population activity at the unstable obstacle locations became more homogeneously elevated across laminae. Altogether, these results support that the hippocampus continues to modulate cortical responses in familiar environments, and the relative impact of descending feedback obeys hierarchical interareal and interlaminar gradients opposite to the flow of ascending sensory inputs.

Key words: cortical layers; motor cortex; place cells; retrosplenial cortex; top–down feedback; two-photon calcium imaging

---

Significance Statement

During learning, the hippocampus imparts spatial context to memory representations throughout the superficial neocortex. However, the postlearning role of the hippocampus has not been well defined. The current results support that, during navigation of a familiar environment, the hippocampus continues to link unreliable sensory attributes to a stable contextual framework, effectively updating the learned model of the environment. The results are also consistent with descending suppression of sensory-evoked activity during behavior, which varied in strength according to hierarchical proximity to the hippocampus. This effect was abolished by bilateral lesions of the dorsal hippocampus, supporting that the hippocampus plays an ongoing role in propagating context-dependent predictions throughout the cortical hierarchy, a core hypothesis of the predictive coding theoretical framework.

Introduction

Fluid spatial navigation relies on an internal representation of space to accurately plan locomotor trajectories, as well as active sensory perception to guide appropriate behavior and flexibly adapt to unexpected perturbations. Hence, as an animal navigates an environment, the neocortex must actively integrate previously learned spatial context with current experience. The integration of diverse feedforward ("bottom–up") and feedback ("top–down") inputs is supported by both regional and laminar organizational hierarchies (Felleman and Van Essen, 1991; Douglas and Martin, 2004; Schwindel and McNaughton, 2011). In brief, unimodal sensory inputs—first relayed by the thalamus to the granular layer of lower-level primary cortices—are cross-modally integrated in higher-level association cortices. This highly processed information ultimately converges on the hippocampus, which possesses an abundance of activity-modifiable synapses that can support rapid associative learning (Monaghan and Cotman, 1985; Moriyoshi et al., 1991; Brose et al., 1993). Thus, at the apex of the cortical hierarchy, hippocampal output can link together the diverse attributes of experience, distributed widely throughout the cortex, within a unique contextual framework (Nadel and Willner, 1980; Teyler and DiScenna, 1986).

The hippocampal code is proposed to facilitate the reinstatement of distributed cortical traces of experience and to orchestrate gradual changes in cortical connectivity for long-term memory consolidation (Marr, 1971; Teyler and DiScenna, 1986; Buzsáki, 1989; Treves and Rolls, 1994; McClelland et al., 1995; Squire and Alvarez, 1995; Takehara-Nishiuchi and McNaughton, 2008). During subsequent slow-wave sleep or quiet wakefulness, the sequences of neural activity that occurred during awake behavior are simultaneously "replayed" in both the hippocampus (Wilson and McNaughton, 1994; Skaggs and McNaughton, 1996; Kudrimoti et al., 1999) and the neocortex (Qin et al., 1997; Euston et al., 2007; Ji and Wilson, 2007; Peyrache et al., 2009). In addition, hippocampal neuronal populations encode unexplored spatial trajectories during replay events (Gupta et al., 2010) and possible future trajectories ahead of behavior (Johnson and Redish, 2007; Pfeiffer and Foster, 2013), implicating the hippocampus in internal model-based planning and higher-level cognition.

Accordingly, descending hippocampal feedback has been shown to influence the functional properties of cortical neurons. Akin to hippocampal place cells (O'Keefe and Dostrovsky, 1971; O'Keefe, 1976; Wilson and McNaughton, 1993), large fractions of cells in the superficial retrosplenial cortex (RSC), primary motor cortex (M1), secondary motor cortex (M2), primary somatosensory cortex (S1), posterior parietal cortex, medial prefrontal cortex, and primary visual cortex (V1) exhibit position-correlated activity during navigation (Fujisawa et al., 2008; Mao et al., 2017; Saleem et al., 2018; Zielinski et al., 2019; Esteves et al., 2021; Gianatti et al., 2023). The emergence of spatially uniform representations of novel environments in the cortex was recently shown to be impeded by bilateral lesions of the hippocampus (Mao et al., 2018; Esteves et al., 2021). Nevertheless, cortical spatial representations of familiar environments largely survive such lesions, a defining characteristic of memory consolidation (Esteves et al., 2023). However, the relative encoding of the spatial context versus the sensory content of experience, and whether the hippocampus continues to modulate the properties of position-correlated cortical cells in familiar environments, remains poorly understood.

To disentangle the relative contributions of learned spatial context (descending "where" information) versus current sensory experience (ascending "what" information) to the activity of cortical cells, neural activity was assessed in dysgranular RSC, posteromedial M2, and forelimb M1 during mouse behavior in a familiar, cued treadmill environment. Together, these regions constitute a spatiomotor network that adheres to conserved interareal pathways of feedforward (M1 → M2 → RSC) and feedback (RSC → M2 → M1) information flow in the cortex (Ueta et al., 2014; Yamawaki et al., 2016). By interchanging the location of two salient cues, sensorimotor activity could be dissociated from global location-specific activity, enabling quantification and characterization of place- and cue-tuned cells throughout the cortical hierarchy. The experimental paradigm was then replicated after bilateral sham or dorsal hippocampal lesions to assess any continued influence of descending feedback from the hippocampus over spatial or cue-based representations of a familiar environment.

Materials and Methods

Animals

A total of 19 adult hemizygous C57BL/6J-Tg(Thy1-GCaMP6s) GP4.3Dkim/J ("Thy1-GCaMP6s"; Jackson Laboratory; RRID, IMSR_JAX:024275) mice were used: 11 males and 8 females (with initial craniotomies completed by 3–4 months of age). Of those 19 mice, 3 (two males and one female) were implanted with a hollow cylinder to enable imaging of the CA1 subregion of the hippocampus. Sixteen mice (nine males and seven females) received a typical cranial window for imaging of cortical regions. Of those latter 16 mice, 10 (six males and four females) received excitotoxic lesions of the dorsal hippocampus, and 6 (three males and three females) received sham lesions after training and prelesion imaging. Age-matched littermates were split equally between the sham and lesion groups and balanced by sex when possible. Following the initial cranial window surgery, mice were housed individually in standard, plastic rodent cages under constant humidity, temperature, and a 12 h light/dark cycle. Mice were experimentally manipulated during the light cycle, and both with food and water were available *ad libitum* throughout the experiment. All procedures were performed in accordance with the Canadian Council on Animal Care guidelines and following protocols approved by the Institutional Animal Care and Use Committee at the University of Lethbridge.

Surgical procedures

Cylinder or cranial window implantation. Before surgery, mice were administered buprenorphine (0.05 mg/kg, s.c.), dexamethasone (2 mg/kg, i.m.), and 0.5 ml of dextrose 5% in water (D5W) with atropine (0.06 mg/kg, s.c.). Mice were then anesthetized with 1.5% isoflurane and immobilized in a stereotaxic frame with body temperature maintained at 37°C by a regulated heating pad. Lidocaine (0.5%, 7 mg/kg, s.c.) was injected under the skin at the incision site. Once the skull was exposed, a custom-made titanium headplate was fixed to the skull using adhesive cement (Metabond, Parkell) and dental acrylic (Jet Tooth Shade Powder and Liquid, Lang Dental Manufacturing).

For imaging of cortical regions, 16 mice were implanted with a standard cranial window. After implantation of the headplate, a bilateral craniotomy, 4 mm in diameter, was performed above the dorsal cortex (centered at the bregma; AP and ML, +2 to −2 mm). Three layers of coverslips (affixed with optical adhesive; NOA71, Norland) were implanted over the craniotomy and attached to the skull with Vetbond (3M). Of the 10 mice in the hippocampal lesion group, 5 were concurrently implanted with both the headplate and the cranial window to enable presurgery imaging (and the coordinates for the bregma were marked on the dental acrylic surrounding the window). However, due to the possibility of cortical distortion interrupting the targeting precision of injections for the lesion surgery, the remaining five mice were initially implanted with a headplate for training and prelesion familiarization with the experimental paradigm, but the cranial window

implantation procedures were postponed and completed with the lesion surgery.

For imaging of CA1, a separate cohort of three mice was implanted with hollow cylinders that afforded unilateral imaging of dorsal CA1. After implantation of the headplate, a 3 mm craniotomy was performed above the right hippocampus (centered at AP, −2.5 mm; ML, −1.5 mm). The cortical tissue was aspirated to a depth of 1 mm, and a hollow glass cylinder (1.5 mm long and 3 mm in diameter) capped with a 3 mm coverslip (affixed with optical adhesive; NOA71, Norland) was inserted until the coverslip touched the exposed cortical white matter. The cylinder was then attached to the skull with Vetbond (3M).

Following implantation of the cylinder or cranial window, dental acrylic was used to create a well around the imaging window, and a rubber O-ring was fixed to the outer edge of the headplate to help retain water during immersion of an objective lens. Mice received injections of meloxicam (Metacam, 1.0 mg/kg, s.c.) and enrofloxacin (Baytril, 10 mg/kg, s.c.) postoperatively and once daily for an additional 3 d following the surgery. Mice were allowed to recover for a minimum of 2 weeks before behavioral training and two-photon microscopy.

Hippocampal excitotoxic and sham lesions. Before surgery, mice were administered phenobarbital (30 mg/kg, i.p.), meloxicam (Metacam, 1 mg/kg, s.c.), dexamethasone (2 mg/kg, i.m.), and 0.5 ml of D5W with atropine (0.06 mg/kg, s.c.). Mice were then anesthetized with 1–1.5% isoflurane and immobilized in a stereotaxic frame with body temperature maintained at 37°C by a regulated heating pad. A dental drill was used to create four small holes (two per hemisphere) in the dental adhesive surrounding the craniotomy and the skull for injection sites targeting the dorsal hippocampal formation (AP, −2.3 mm; ML, ±1.5 mm; DV, 1.8 mm; and AP, −3.2 mm; ML, ±2.5 mm; DV, 2.0 mm; locations of injection sites shown in Fig. 1A). Eight pulses (9.2 nl/pulse for a total of 73.6 nl) of 15 mg/ml N-methyl-D-aspartate (NMDA; Sigma-Aldrich) in 1X phosphate–buffered saline (PBS) were then injected at each site with a Nanoject II autonanoliter injector (Drummond Scientific) and a beveled micropipette (20–30 μm tip diameter) with an interpulse interval of 15 s. For sham lesions, the micropipette was loaded and inserted into the hippocampus at the injection sites, but no pulses were administered. The injection sites were subsequently closed with dental adhesive, and diazepam (5 mg/kg, i.p.) was administered to both sham and lesion animals to prevent seizures. Mice also received injections of meloxicam (Metacam, 1 mg/kg, s.c.) and enrofloxacin (Baytril, 10 mg/kg, s.c.) postoperatively and once daily for an additional 3 d following the surgery. Mice were allowed to recover for a minimum of 21 d to allow sufficient time for NMDA to exert its excitotoxic effects.

Behaviour

Training. During the first 3 d of training, head-fixed mice were acclimatized to a mild, aversive air stimulus and trained to run on a nonmotorized treadmill in response to it (Fig. 1A). An automated solenoid valve-based system was used to direct a continuous air stream from a regulated compressed air supply toward the rump of the mice (Inayat et al., 2023). During these first three training sessions, progressively longer running distances were required to trigger cessation of the air stimulus, at which point the mice could move freely on the belt without the air stimulus for 15 s. After the initial 3 d, the air stimulus duration was increased such that mice had to run one complete lap of the belt (150 cm) to trigger cessation of the air stimulus, at which point a brake was applied to prevent movement during the 15 s intertrial interval. This brake point occurred whenever a photoelectric sensor (Omron) was triggered by a reflective tape attached on the opposite side of the belt and coincided with delivery of a ~1 μl strawberry-flavored milk reward dispensed by a solenoid pinch valve (Bio-Chem). A custom-designed circuit and microcontroller (Arduino Uno, Farnell) were used to control reward delivery, as well as the air stimulus onset and offset. Mice were trained daily for a minimum of 2 weeks and until they consistently ran for 20 min (the duration of a typical imaging session).

The treadmill belt—used for both training and subsequent experiments—was constructed with a 150 cm length of Velcro (Country Brook) and included two static visuotactile cues, hot glue circles and

reflective tape strips, as well as two separate but identical squares of treadmill material that both joined the ends of the belt and marked where two obstacles would later be attached during experiments (Fig. 1B, "static cues only"). Two polyamide wheels (10 cm in diameter) were used to guide the circular treadmill belt, and an optical encoder (Avago Technologies) attached to the wheel shaft was used to monitor the belt movement during behavior.

Experimental paradigm. One region of interest (dorsal CA1, anterior RSC, posteromedial M2, or forelimb M1; Fig. 1A) was imaged for ~20 min per day for 10 consecutive days (Fig. 1B, "experimental paradigm"). For each region of each mouse, the sampled hemisphere was preferentially determined by the clarity of cells (i.e., the hemisphere least obscured by blood vessels or bone regrowth was selected), and the location of the imaging window was kept constant across days. On Days 1–2 and 9–10, mice ran on the familiar treadmill belt used during training (Fig. 1B, "static cues only"). On Days 3 and 8, two additional obstacles —rough Velcro strips (Obstacle A) and a soft block-like barrier (obstacle B)—were added in orientations A/B and B/A, respectively, but remained static throughout these imaging sessions. During Days 4–7, obstacles A and B were added in a pseudorandom order to the treadmill belt, and their positions were interchanged midway through the session (Fig. 1B, "added obstacles"). As during training, mice had to run one complete lap of the belt to trigger cessation of the air stimulus, at which time the brake was applied, a milk reward was delivered, and there was a 15 s intertrial rest interval. Mice were given a minimum of 3 d of rest after completion of the 10 d paradigm before another cortical region was imaged using the same methods. The order that each region of interest was imaged was varied across mice. The aforementioned protocol was then repeated for each region of interest after bilateral sham or dorsal hippocampal lesions.

Two-photon microscopy

Images were acquired using a Thorlabs Bergamo II multiphoton microscope. A Ti:sapphire femtosecond pulsed laser (Coherent Chamelion Ultra II)—tuned to an excitatory wavelength of 920 nm—was passed through a 16× water immersion objective (Nikon; NA, 0.8; 80–120 mW output power measured at the sample). Using a galvo-resonant scanner and a piezoelectric oscillator, 12 836 μm × 418 μm planes, each separated in the z-dimension by 35 μm and spanning a total depth of 385 μm across Layers II–V of the cortex, were sequentially acquired (Fig. 1C). Emitted signals were amplified using a GaAsP photomultiplier tube (Hamamatsu Photonics), and each frame was digitized to a resolution of 384 × 192 pixels at a sampling rate of 5 Hz. For dorsal CA1, the galvo-resonant scanner was used to acquire a single 835 μm × 835 μm plane, which was digitized to a resolution of 800 × 800 pixels at a sampling rate of 19 Hz. Photosensor and rotation encoder signals were acquired and synchronized with imaging data using a data acquisition system (Axon Instruments Digidata 1322A) and Clampex software (Axon Instruments). During imaging, a strip of Velcro was wrapped around the body of the objective and lowered to the level of the cranial window to block ambient light.

Histology

During sacrifice, mice were deeply anesthetized with an intraperitoneal injection of sodium pentobarbital (1,000 mg/kg) and perfused transcardially with 1X PBS and 4% paraformaldehyde (PFA; Sigma-Aldrich). Following fixation, brains were extracted, postfixed overnight in 4% PFA, and subsequently cryoprotected in 30% sucrose in 1X PBS with 0.02% sodium azide. Coronal sections (40 μm) were prepared using a sliding microtome (Model 860; American Optical Instrument). Sections were collected in 1X PBS, manually mounted on Superfrost Plus slides (Thermo Fisher Scientific), and dried before coverslipping with VECTASHIELD Antifade Mounting Medium (Vector Laboratories).

A NanoZoomer (Hamamatsu Photonics) scanning microscope was then used to acquire images of all coronal sections. For both sham and lesion mice, the area of the intact hippocampus and subiculum in each hemisphere of each section was measured using the freehand region

drawing tool in the NDP.view2 image viewing software (Version 2.3.1; Hamamatsu Photonics). The total volume of the intact hippocampus and subiculum per hemisphere was then calculated by multiplying the observed area in each section by the section thickness (40 μm) and summing the resulting volumes across all sections. Mice with dorsal lesions that comprised <50% of the total mean volume of intact (sham) hippocampi (including dorsal and ventral regions) were excluded from postlesion analyses (Fig. 1D).

Image processing and analysis
Suite2p was used for automated image registration, cellular ROI detection, and activity extraction (Pachitariu et al., 2016). For all datasets, the most superficial two planes and all flyback frames were excluded from analyses. For each brain region of each animal, both the reference images from each movie and all automatically detected cellular ROIs were registered across all experimental days, and raw activity traces were concatenated. For imaging frames that could be accurately aligned before and after the lesion surgeries, reference images and cellular ROIs were registered across all presurgery and postsurgery days. Among all automatically detected cellular ROIs, those that fell below a 50% probability of being a cell (relative to the classifier) were excluded. The remaining cellular ROIs were then manually assessed by one researcher, blind to the treatment group, to exclude cell bodies that were duplicated, incompletely segmented, or whose raw activity trace did not exhibit distinct calcium fluorescence peaks that were greater in magnitude than the baseline signal.

Raw fluorescence traces were extracted for each cellular ROI by averaging the fluorescence of all pixels within the ROI and subtracting the neuropil and baseline signals as in Esteves et al. (2023). Briefly, to determine neuropil contamination, each ROI mask was dilated by 8 pixels, and the original ROI mask, dilated by 1 pixel, was subtracted. The raw neuropil fluorescence was calculated as the mean fluorescence of the remaining ring mask, and singular value decomposition was used to reconstruct the timeseries of neuropil fluorescence for each ROI. For each raw fluorescence trace (F), a rolling baseline (F_0) was estimated with a Gaussian filter (10 s width), which was then minimum and maximum filtered with a 60 s window. This baseline was then subtracted from the raw fluorescence signal $[(F - F_0)/F_0]$, and deconvolved spike rates were computed from the extracted $\Delta F/F_0$ traces by a constrained non-negative matrix factorization algorithm (Pnevmatikakis et al., 2016; Fig. 1E). All subsequent analyses were completed using the deconvolved activity traces (without normalization, unless otherwise specified).

Position-correlated cells were identified as previously described (Chang et al., 2020; Esteves et al., 2021) using custom-written MATLAB (MathWorks; version R2019a) code. Briefly, two criteria needed to be met for a neuron to be classified as position-correlated. First, the spatial information (SI) conveyed by a neuron about the animal's location needed to exceed the 95th percentile of a shuffled distribution. Spatial information was computed as in Skaggs et al. (1993) as follows:

$$\text{SI} = \sum_{i=1}^{N} p_i \frac{f_i}{f} \log_2 \frac{f_i}{f},$$

where the average neuronal activity (f_i) in the ith bin over the total average activity (f), weighted by the occupancy (p_i), was evaluated over $N = 50$ spatial bins (one bin, 3 cm). The null distribution of SI was obtained by circularly shifting the timecourse vectors of neuronal activities 1,000 times by a random factor. Second, the place fields of neurons were identified by conducting a continuous wavelet transform over the spatial tuning curve using a Ricker (Mexican Hat) wavelet. The scales evaluated were $\Sigma = \{1, 2, 3, …, 50\}$ corresponding to the $N = 50$ spatial bins. Local maxima exceeding 3 median absolute deviations from the wavelet coefficients at the lowest scale of the transform ($\sigma = 1$) were identified as potential place fields. If a local maximum fell within the bounds of another maximum at a higher scale (i.e., a wider place field), the candidate with the narrower place field was discarded. The width of a place field was restricted between 5 and 80% of the length

of the environment, and the mean activity within a place field had to be 2.5 times higher than the activity outside of place fields. Peak activity during individual trials must also have occurred within the place field in at least a third of the total trials. Cells that exhibited one or more place fields satisfying these criteria were considered to be position-correlated.

For differentiation of cue- and place-tuned cells, analyses were restricted to position-correlated cells that had place fields within the 18 cm trailing the leading edge of each of the interchangeable obstacles. Cue cells were defined as those position-correlated cells that exhibited maximum mean normalized activity at the position of one specific obstacle across Days 3–8, regardless of its location on the track, whereas place cells were defined as position-correlated cells that always exhibited maximum mean normalized activity at the same location on the track, regardless of which obstacle was present.

Lifetime sparsity—a measure of how diffuse the firing of an individual neuron is in the spatial domain—was calculated as in Jung et al. (1994) as follows:

$$\text{sparsity} = \frac{(\sum_{i=1}^{N} p_i f_i)^2}{\sum_{i=1}^{N} p_i f_i^2},$$

where f_i is the average neuronal activity in the ith bin, weighted by the probability of occupancy (p_i), and evaluated over $N = 50$ spatial bins. Sparsity ranges between 0 and 1, where smaller values indicate narrower spatial tuning profiles (i.e., firing was more sparse).

Population activity was decoded using an independent Bayesian decoding algorithm (Zhang et al., 1998; Mao et al., 2018; Esteves et al., 2021, 2023). Briefly, the maximum log-posterior probability of being at a position (x) given the population response of all imaged neurons was estimated as follows:

$$\max_{x} l\left(\frac{x}{n}\right) \propto \sum_{i=1}^{N} n_i \log(f_i(x)) - \delta t \sum_{i=1}^{N} f_i(x) + \log(P(x)),$$

where $f_i(x)$ is the mean deconvolved fluorescence trace of neuron i at position x, n_i is the timecourse vector of the ith neuron within a time bin of length $\delta t = 1$ s, N is the number of neurons, and $P(x)$ is the probability of occupancy at position x. To control for differences in total detected neurons between subjects and regions, the M-out-of-N bootstrap method (Bickel and Sakov, 2008; Yong et al., 2022) was used to estimate the distribution of decoding error on a single test day (Day 8; with added obstacles in a stable orientation), where $M = 250$ neurons were sampled from N total cells with replacement. To avoid a sampling bias that can emerge when M approaches N, six (out of 50) datasets were excluded from these analyses because they contained <350 total detected cells. Decoding accuracy was assessed using leave-one-out cross-validation. Given k trials, $k - 1$ trials were used to calculate the likelihood ($f_i(x)$) and prior ($P(x)$) probabilities, and n_i from the omitted trial was used to evaluate the decoding error. This process was repeated for all k trials. Decoded position was defined as the position with the highest probability for any given time bin, and the Bayesian decoding error was the absolute value of the difference between true position and decoded position.

Statistical analyses were performed using MATLAB (MathWorks; version R2019a) and GraphPad Prism (version 9.4.1). For repeated-measure analysis of variance (ANOVA) calculations, sphericity was not assumed, and the Geisser–Greenhouse correction was applied, if necessary. The Tukey–Kramer test was used to correct for multiple comparisons in instances where all means from all groups were compared, and the Dunn–Šidák correction was applied when only select subsets of the group means were compared.

Results

Two-photon microscopy was used to longitudinally image neurons from male and female genetically encoded Thy1-GCaMP6s calcium indicator mice during running on a cued, nonmotorized
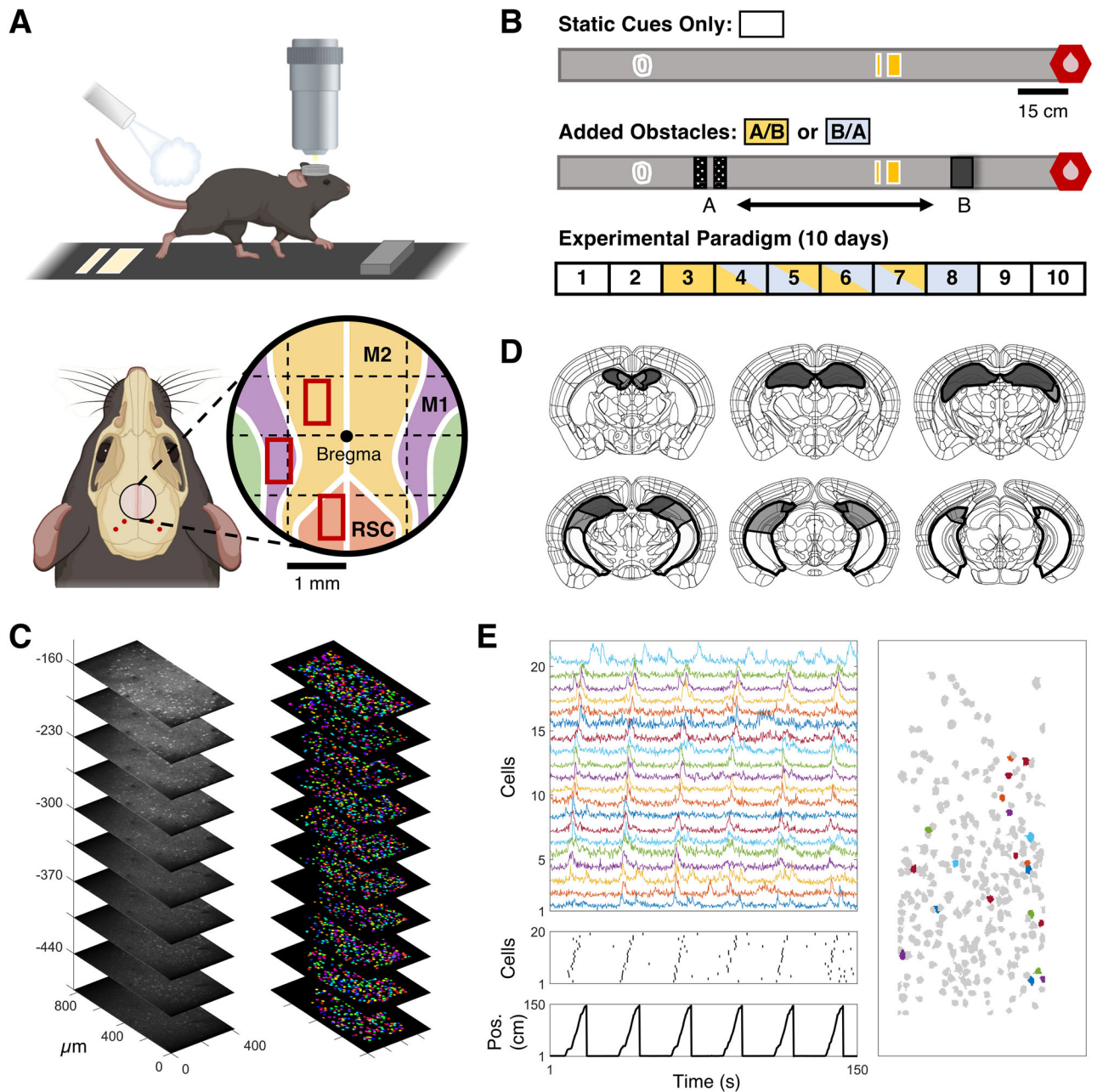
Figure 1. Overview of the experimental paradigm and two-photon imaging of the neocortex. ***A***, Top, Schematic diagram of a head-fixed mouse on the treadmill belt situated under a two-photon microscope. A mild aversive air stimulus directed at the rump was used to motivate running. Bottom, Cortical regions of interest within the cranial window area and example positions of the 417 μm × 835 μm imaging frames (red rectangles) over anterior RSC, posteromedial M2, and forelimb M1. Red dots indicate NMDA and sham injection sites. Figure created with BioRender.com. ***B***, The 150 cm treadmill belt had two static cues (reflective tape strips and glue circles) and two interchangeable obstacles (A, rough Velcro strips and B, a raised block) that were added in the indicated positions during the 10 d experimental paradigm. After each complete lap, a brake was applied for 15 s, the air stimulus was turned off, and mice received a ~1 μl strawberry milk reward. On Days 1–2 and 9–10, mice ran on the familiar treadmill belt without added obstacles. On Days 3 and 8, the obstacles were added in orientations A/B and B/A, respectively, but remained static throughout the imaging session. On Days 4–7, the obstacles were pseudorandomly added to the treadmill belt, and their position was interchanged midway through the session. The same protocol was applied before and after bilateral sham or dorsal hippocampal lesion surgeries. ***C***, Schematic depictions of the maximum extent (shaded gray) and minimum extent (dark gray) of dorsal hippocampal lesions included in the experiment. Note that the dorsal subiculum was also lesioned. Figure adapted from the Allen Mouse Brain Atlas (Lein et al., 2007; Allen Brain Institute for Science, 2011). ***D***, Example maximum intensity projection z-stack from M2 spanning 10 frames from −160 to −475 μm below the cortical surface (left) and the corresponding Suite2p-detected neurons (right). ***E***, Raw, normalized $\Delta F/F_0$ traces (top left) and raster plot of corresponding deconvolved traces (middle left) relative to animal position (Pos.; bottom left) of 20 example place cells detected within one imaging plane ($x = 417$ μm; $y = 835$ μm; $z = -190$ μm; right panel) from RSC.

treadmill. During active behavior, each cortical region of interest (anterior dysgranular RSC, posteromedial M2, or forelimb M1) was imaged for 10 consecutive days (Fig. 1*A*). On select days, two added obstacles interchanged locations midway through behavior to decouple location-specific activity from sensorimotor

activity, which enabled detection and characterization of place- and cue-tuned cell subtypes at those locations (Fig. 1*B*). To enable assessment of both superficial and deep layer cells, 10 planes were imaged spanning layers II–Va (LII–Va) of motor cortices (Fig. 1*C*). However, due to anatomical limitations, imaging planes were

restricted to superficial layers (LII–III) of dysgranular RSC. To examine any continued influence of the hippocampus on familiar spatial representations, the experimental paradigm was then replicated for each cortical region of interest after mice received sham or complete, bilateral dorsal hippocampal lesions (Fig. 1D). Active neurons were automatically detected and registered across days (Fig. 1C), and large fractions of cortical cells were found to be selectively tuned to precise positions within the treadmill environment, analogous to hippocampal "place cells" (Fig. 1E). For comparison of cortical cells with hippocampal cells, dorsal CA1 was imaged in a separate cohort of mice according to the same experimental paradigm.

Use of an aversive air stimulus improves running performance

The treadmill environment included two static somatosensory cues, which remained in fixed positions throughout the experimental timeline, and two additional obstacles that were added, interchanged, or removed from the treadmill belt on select days (Fig. 2A). Relative to the static cues, the added obstacles were larger to ensure that mice made tactile contact with them during running. However, these obstacles also made the treadmill environment more physically demanding to traverse, which impaired performance among mice motivated by reward alone (Fig. 2B). Thus, as an alternative to conventional chronic water restriction and reward-motivated behavior (Mao et al., 2017,
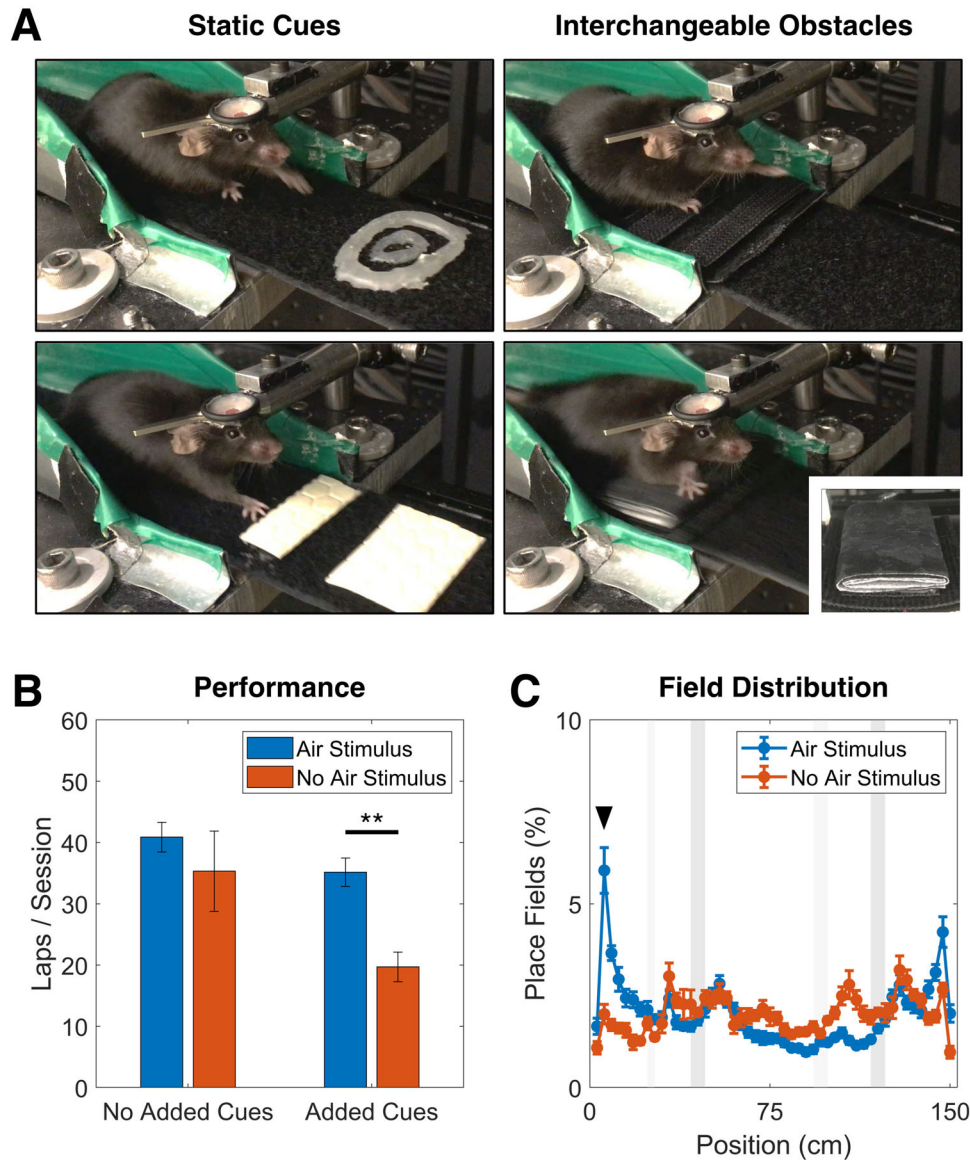

Figure 2. An aversive air stimulus improved running performance in physically demanding environments, and the air stimulus onset was overrepresented as a salient sensory cue. *A*, The treadmill belt—used for both training and subsequent experiments—was a 150 cm length of soft Velcro that included two static visuotactile cues: hot glue circles (top left) and reflective tape strips (bottom left). During Days 3–8 of the experimental paradigm, two obstacles were added to the belt that interchanged positions: rough Velcro strips (top right) and a soft block-like barrier (bottom right; inset shows side view). Note that the Velcro strips were not a purely tactile cue but required a pulling motion during traversal due to friction from the barrier on the opposite side of the belt as it passed through the open braking system. In these images, the objective lens, second headplate stabilizing bar, and the reward delivery system were removed from the apparatus for clarity. *B*, Number of laps (averaged over three days) run by mice in response to an aversive air stimulus (blue) relative to reward motivation only (orange) in the presence and absence of the added interchangeable obstacles. Error bars are SEM across mice. See Table 1 for summary of statistics. *C*, Distributions of place field locations across the binned length of the treadmill belt in mice running in response to an aversive air stimulus (blue) relative to reward motivation only (orange). The air stimulus onset is located at the first binned position in the treadmill environment (corresponding peak in place field distribution indicated by black arrowhead). Gray bars indicate positions of stable cues (light gray) and interchangeable obstacles (dark gray). Error bars are SEM across mice.

2018; Esteves et al., 2021, 2023), treadmill running was motivated by a mild, aversive air stimulus. In the presence of the added obstacles, the use of the air stimulus significantly increased the number of trials performed relative to mice motivated by reward alone (Fig. 2B). Consistent with other studies that employed an aversive air stimulus (Okada et al., 2017; Inayat et al., 2023), spatial resolution was increased near the location of the air stimulus onset/offset (Fig. 2C), akin to the overrepresentation of place fields at the locations of rewards, goals, or other salient sensory cues (Hollup et al., 2001; Burke et al., 2011; Gauthier and Tank, 2018; Bourboulou et al., 2019; Sato et al., 2020). Notably, these fields were largely absent when mice were motivated by the coincident strawberry milk reward only (Figs. 1B, 2C), supporting that the air stimulus was preferentially utilized as a salient sensory cue at this location.

Position-correlated cortical cells encode lower spatial information than hippocampal "place" cells

Many recent studies have identified spatially tuned cortical cells, and these have been posited to be cortical correlates of hippocampal place cells (Fujisawa et al., 2008; Mao et al., 2017; Saleem et al., 2018; Zielinski et al., 2019; Esteves et al., 2021; Gianatti et al., 2023). Accordingly, in the current study, large proportions of active cells in anterior RSC, posteromedial M2, and forelimb M1 were found to exhibit position-correlated activity, and these cells comprised sequences that uniformly tiled the treadmill environment (Figs. 1E, 3A–C). However, few studies have concurrently compared the spatial characteristics of position-correlated cortical and hippocampal cells. To address this gap in the literature, we imaged dorsal CA1 in a small cohort of mice ($n = 3$) according to the same experimental paradigm. Notably, position-correlated cells in CA1 encoded significantly higher spatial information (Fig. 3D) and lower lifetime sparsity indices (Fig. 3E) relative to all examined cortical regions, which is likely a consequence of lower out-of-field activity (Fig. 3B). Alternatively, spatial information measures can be biased by the slow, nonlinear rise and decay rates of fluorescence transients. While the Skaggs et al. (1993) metric has proven to be the most robust approach to analysis of calcium imaging data, there is an increasing error associated with slower calcium indicators and cells encoding higher information (when measured in bits/action potential; Climer and Dombeck, 2021). However, spatial information saturates logarithmically, and the median fluorescence of cells in hippocampal CA1 was significantly lower than that of cortical cells (Fig. 3D, inset), supporting that there was a true difference in spatial information between hippocampal and cortical cells. Notably, there were no significant differences across cortical regions in the median fluorescence of all position-correlated cells (Fig. 3D, inset) or cells without position tuning (data not shown; see Table 1 for summary of statistics), consistent with previous findings that the properties of GCaMP6s fluorescent transients do not significantly vary across cortical regions (Gianatti et al., 2023). Besides spatial information and lifetime sparsity, position-correlated cell characteristics were otherwise comparable across regions, including place field distribution (Fig. 3F), place field width (Fig. 3G), and the fraction of position-correlated cells exhibiting only one place field (or, conversely, multiple fields; Fig. 3H). These findings suggest that neuronal populations in hippocampal CA1 and cortical regions each encode analogous representations of the environment, but position-correlated cells in the dorsal cortex appear to be less rigidly tuned than those in dorsal CA1. However, care should be taken to avoid generalizing these results to the entire

hippocampal formation as the spatial properties of hippocampal (and subicular) cells vary along the septotemporal axis (Barnes et al., 1990; Jung et al., 1994; Kim et al., 2012).

Neocortical spatial representations of familiar environments persist after hippocampal lesions

In mice that were introduced to a novel environment, Esteves et al. (2021) demonstrated that bilateral hippocampal lesions significantly decreased both the detected proportion of position-correlated cortical cells and their encoded spatial information relative to sham controls, which was interpreted as a failure to acquire a cortical representation of the novel spatial environment. However, in a subsequent study, Esteves et al. (2023) reported that spatial tuning was preserved in a preoperatively learned environment. Thus, to validate the persistence of cortical spatial representations of a learned environment after hippocampal lesions, we next quantified the general characteristics of position-correlated cells in cortical regions before ($n = 11$) and after bilateral sham ($n = 5$) or dorsal hippocampal lesions ($n = 4$). Across cortical regions, there were no generalized effects of lesion on the fraction of position-correlated cells recruited on any given day (Fig. 4A), encoded spatial information (Fig. 4B), lifetime sparsity (Fig. 4C), field distribution (Fig. 4D), field width (Fig. 4E), or the number of fields detected per cell (Fig. 4F). However, relative to when only the static cues were present, the addition of the interchangeable obstacles significantly increased spatial information (Fig. 4B) and decreased lifetime sparsity (Fig. 4C) and median place field width (Fig. 4E) across the position-correlated cell populations of all lesion groups. Finally, a Bayesian decoder was used to decode mouse position from population activity. Among presurgery mice, median decoding error was lowest in hippocampal CA1 ($M \pm SD$ across mice, 3.20 ± 0.32 cm) and consistently increased across cortical regions with hierarchical distance from the hippocampus (RSC, $M \pm SD = 5.75 \pm 3.90$ cm; M2, $M \pm SD = 7.75 \pm 3.90$ cm; M1, $M \pm SD = 9.52 \pm 4.00$ cm). However, the median decoding error was not significantly different between cortical regions or lesion groups (Fig. 5). Consistent with enhanced spatial information and reduced place field width after addition of the interchangeable obstacles, the decoding error was specifically reduced trailing the locations of the two interchangeable obstacles across all cortical regions and treatment groups. Taken together, these results support that (1) spatial representations of the familiar environment persisted after bilateral hippocampal lesions, (2) the addition of local cues generally enhanced cortical spatial representations of a familiar environment, and (3) the use of an aversive air stimulus did not differently affect the spatial properties of cells compared with previous studies that employed reward-motivated running.

It is important to note, however, that there was a main effect of the treatment group on the total number of cells detected per mouse such that significantly fewer cortical cells were active in mice with bilateral dorsal hippocampal lesions relative to both presurgery and sham controls (Fig. 6A). There was substantial uncontrolled variability in the total number of detected cells between individual mice (and between regions within subjects) due to differences in the extent that blood vessels, the edge of the cranial window, or bone regrowth obscured individual imaging frames. Nevertheless, lesioned mice exhibited a significantly lower density of detected cells than both presurgery and sham controls (Fig. 6B), a result that could not be explained by gross motor deficits. Relative to presurgery and sham controls, running performance was not impaired by complete bilateral
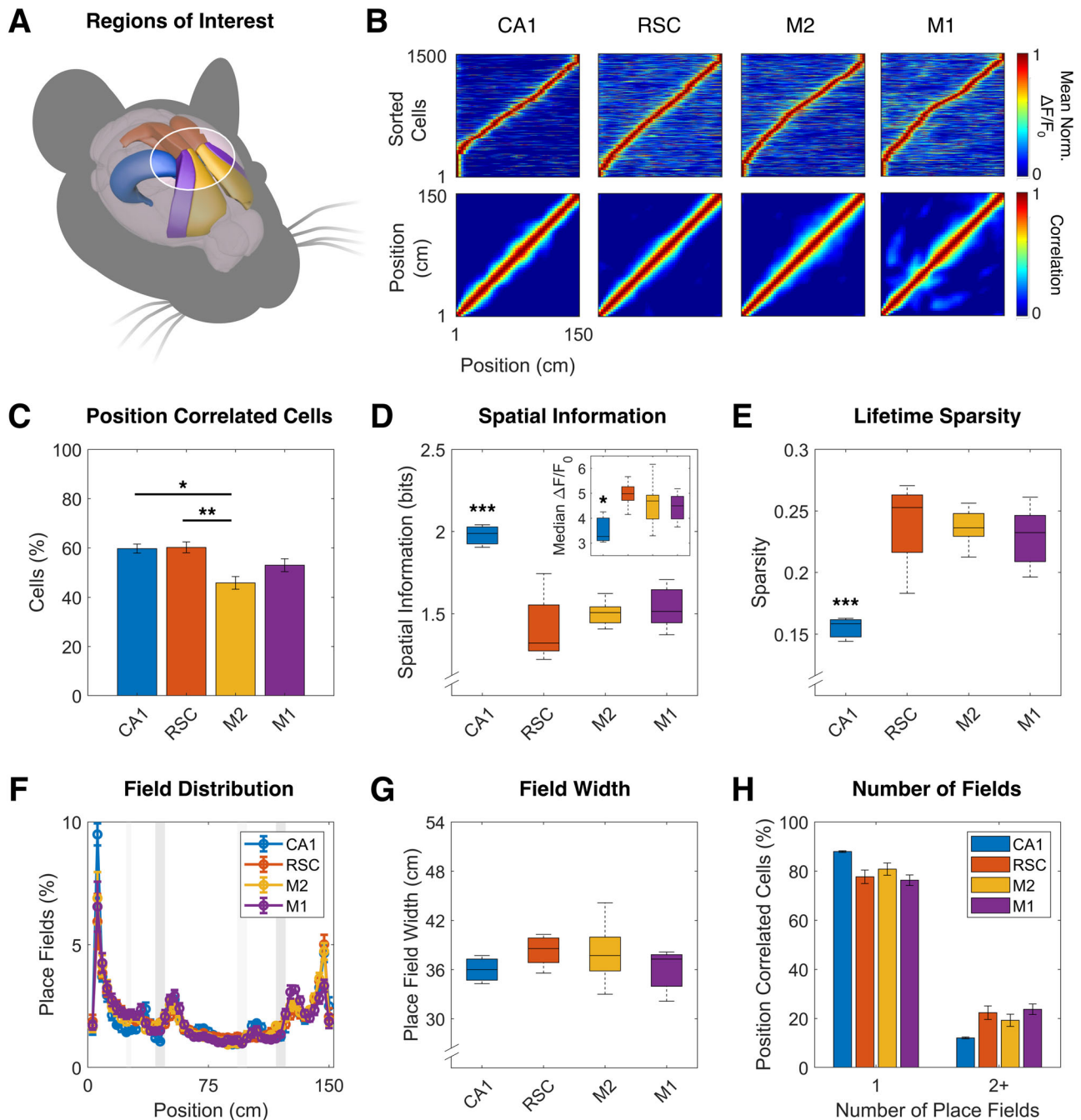
Figure 3. Comparison of presurgery position-correlated cell characteristics in hippocampal CA1 and cortical regions (RSC, M2, and M1). **A**, Regions of interest: dorsal CA1 of the hippocampus (blue), anterior RSC (orange), posteromedial M2 (yellow), and hindlimb M1 (purple). Figure created with the Scalable Brain Atlas (Lein et al., 2007; Bakker et al., 2015). The dorsal position of the imaging window above these regions is shown as a white circle (not to scale). **B**, Top, Position-correlated cells were pooled across mice, and a random selection of 1,500 cells was sorted by the order of maximum mean normalized $\Delta F/F_0$ on a day with static cues only. Bottom, Pearson's correlation matrices of sorted cells. **C**, Proportions of all detected cells that were classified as position correlated. Error bars are SEM across mice. **D**, Median spatial information encoded by position-correlated cells. Inset shows median non-normalized $\Delta F/F_0$ across position-correlated cells. For all boxplots, line, median; box, 25th and 75th percentiles; whiskers, minimum and maximum values; + signs, outliers. **E**, Median lifetime sparsity of position-correlated cells. **F**, Binned distributions of place field locations across the length of the treadmill belt. Gray bars indicate positions of stable cues (light gray) and interchangeable obstacles (dark gray). Error bars are SEM across mice. **G**, Median place field width of position-correlated cells. **H**, Fractions of position-correlated cells with one or more (2+) place fields. Error bars are SEM across mice. Note: for **C–H**, measures were averaged across all presurgery experimental days for each mouse. Refer to Table 1 for a summary of statistics.

dorsal hippocampal lesions as there were no significant differences in the mean running velocity per trial or in the mean number of trials performed over a 20 min period (Fig. 6C). Although inactive cells were not quantified in this study, these findings suggest that complete dorsal hippocampal lesions may impair cortical cell recruitment during navigation

of a familiar environment. However, such a hippocampal effect on cell recruitment has not been reported by other studies that used comparable methods (Mao et al., 2018; Esteves et al., 2021, 2023), and, thus, uncontrolled variability among mice cannot be excluded as the underlying cause of this disparity between experimental groups.

Table 1. Summary of statistics

Figure	Variable	Statistical test(s) and results
Figure 2A	Number of trials performed with added obstacles	$M \pm SD$, air stimulus motivated, 35 ± 8 laps; reward-motivated: 20 ± 6 laps; two-tailed t test; $t_{(11)} = 4.0505$; $p = 0.0019$
Figure 3C	Fraction of position-correlated cells (by region)	One-way ANOVA, $F_{(3,27)} = 6.718$; $p = 0.0016$; Tukey's test, M2 and RSC: $p = 0.0016$; M2 and CA1, $p = 0.0377$
Figure 3D	Spatial information (by region)	One-way ANOVA and Tukey's test; $F_{(3,27)} = 15.56$; $p < 0.0001$
Figure 3D inset	Median fluorescence (by region and cell tuning)	Two-way repeated–measure ANOVA Main effect of region: $F_{(3,28)} = 5.697$; $p = 0.0036$; Dunn–Šidák test, CA1 and RSC, $t_{(28)} = 3.154$; $p = 0.023$; CA1 and M2, $t_{(28)} = 4.120$; $p = 0.0018$; CA1 and M1, $t_{(28)} = 3.360$; $p = 0.014$; No main effect of cell tuning (position vs none), $F_{(1,28)} = 0.6803$; $p = 0.42$
Figure 3E	Lifetime sparsity (by region)	One-way ANOVA, $F_{(3,27)} = 12.21$; $p < 0.0001$; Tukey's test, CA1 and RSC/M2/M1, $p < 0.0001$
Figure 3F	Place field distribution (by region)	Two-sample χ^2 tests and Bonferroni's corrected $a = 0.01$; $p = 0.02–0.45$
Figure 3G	Place field width (by region)	One-way ANOVA, $F_{(3,27)} = 1.336$; $p = 0.28$
Figure 3H	Fraction of position-correlated cells with >1 place field (by region)	One-way ANOVA, $F_{(3,27)} = 1.846$; $p = 0.11$
Figure 4A	Fraction of position-correlated cells (by lesion and cues present)	Two-way repeated-measure ANOVAs No effect of lesion: RSC, $F_{(2,11)} = 0.9978$; $p = 0.40$; M2, $F_{(2,17)} = 0.8760$; $p = 0.43$; M1, $F_{(2,13)} = 0.2484$; $p = 0.78$; No main effect of cues present: RSC, $F_{(1,11)} = 0.0917$; $p = 0.77$; M1, $F_{(1,13)} = 1.9070$; $p = 0.19$; Main effect of cues present: M2, $F_{(1,17)} = 10.39$; $p = 0.005$; Dunn–Šidák test, lesion, $t_{(17)} = 3.249$; $p = 0.01$
Figure 4B	Spatial information (by lesion and cues present)	Two-way repeated–measure ANOVAs No main effect of lesion: RSC, $F_{(2,11)} = 0.6590$; $p = 0.54$; M2, $F_{(2,17)} = 0.1680$; $p = 0.85$; M1, $F_{(2,13)} = 0.6660$; $p = 0.53$; Main effect of cues present: RSC, $F_{(1,11)} = 145.1$; $p < 0.0001$; M2, $F_{(1,17)} = 254.2$; $p < 0.0001$; M1, $F_{(1,13)} = 156.6$; $p < 0.0001$
Figure 4C	Lifetime sparsity (by lesion and cues present)	Two-way repeated-measure ANOVAs No main effect of lesion: RSC, $F_{(2,11)} = 0.4208$; $p = 0.67$; M2, $F_{(2,17)} = 1.003$; $p = 0.39$; M1, $F_{(2,13)} = 0.4364$; $p = 0.66$; Main effect of cues present: RSC, $F_{(1,11)} = 72.39$; $p < 0.0001$; M2, $F_{(1,17)} = 158.8$; $p < 0.0001$; M1, $F_{(1,13)} = 157.2$; $p < 0.0001$
Figure 4D	Place field distribution (by lesion)	Two-sample χ^2 tests, RSC, $p = 0.08–0.39$; M2, $p = 0.29–0.34$; M1, $p = 0.08–0.33$
Figure 4E	Place field width (by lesion and cues present)	Two-way repeated–measure ANOVAs No main effect of lesion: RSC, $F_{(2,11)} = 0.7071$; $p = 0.51$; M2, $F_{(2,17)} = 0.1246$; $p = 0.88$; M1, $F_{(2,13)} = 0.7417$; $p = 0.50$; Main effect of cues present: RSC, $F_{(1,11)} = 39.43$; $p < 0.0001$; M2, $F_{(1,17)} = 17.13$; $p = 0.0007$; M1, $F_{(1,13)} = 52.74$; $p < 0.0001$
Figure 4F	Fraction of position-correlated cells with >1 place field (by region and lesion)	Two-way ANOVA No main effect of region: $F_{(2,41)} = 1.166$; $p = 0.3218$; Main effect of lesion: $F_{(2,41)} = 4.828$; $p = 0.01$; Tukey's test, RSC, $p = 0.25–0.85$; M2, $p = 0.35–0.99$; M1, $0.14–0.83$
Figure 5A	Bayesian decoding error (by region and lesion)	$M \pm SD$, CA1, 3.20 ± 0.32 cm; RSC, 5.75 ± 3.90 cm; M2, 7.75 ± 3.90 cm, M1, 9.52 ± 4.00 cm; Two-way ANOVA No main effect of region: $F_{(2,35)} = 1.4250$; $p = 0.25$ No main effect of lesion: $F_{(2,35)} = 1.9640$; $p = 0.16$
Figure 6A	Total detected cells (by lesion)	One-way ANOVA, $F_{(2,47)} = 6.963$; $p = 0.0022$
Figure 6B	Distance between detected cells and nearest 3 neighbors (by lesion)	One-way ANOVA, $F_{(2,47)} = 17.95$; $p < 0.0001$; Tukey's test, lesion, and presurgery, $p < 0.0001$; lesion and sham, $p = 0.0002$
Figure 6C	Running velocity per trial (by lesion)	One-way ANOVA, $F_{(2,17)} = 0.1542$; $p = 0.86$
Figure 6C inset	Number of trials performed per ~20 min (by lesion)	One-way ANOVA, $F_{(2,17)} = 0.3244$; $p = 0.68$
Figure 8B	Mean non-normalized peak activity before and after cue-swaps (Note: peak activities of individual example cells are shown; statistics compare population means across mice)	Paired two-tailed t tests Place cells, $t_{(27)} = 5.6865$; $p < 0.0001$; Cue cells, $t_{(27)} = 0.4653$; $p = 0.65$; Place cells at nonpreferred obstacle location (relative to baseline), $t_{(27)} = 6.5169$; $p < 0.0001$; Cue cells at nonpreferred obstacle (relative to baseline), $t_{(27)} = 5.1182$; $p < 0.0001$
Figure 9A	Fraction of cue cells at obstacle locations (by region)	One-way ANOVA, $F_{(2,25)} = 31.67$; $p < 0.0001$; Tukey's test, M1 and M2, $p = 0.0029$; M1 and RSC, $p < 0.0001$; M2 and RSC, $p = 0.0002$; Data not shown: CA1 and RSC, two-tailed t test, $t_{(9)} = 1.1$; $p = 0.30$
Figure 9B	Spatial information of place or cue cells (by region)	One-way ANOVAs Place cells, $F_{(2,25)} = 2.846$; $p = 0.08$; Cue cells, $F_{(2,25)} = 6.385$; $p = 0.0058$; Tukey's test, RSC and M2, $p = 0.0366$; RSC and M1, $p = 0.0052$
Figure 9C	Lifetime sparsity of place or cue cells (by region)	One-way ANOVAs Place cells, $F_{(2,25)} = 1.055$; $p = 0.36$; Cue cells, $F_{(2,25)} = 4.046$; $p = 0.03$; Tukey's test, RSC and M2, $p = 0.14$; RSC and M1, $p = 0.0257$

(Table continues.)

Table 1. Continued

Figure	Variable	Statistical test(s) and results
Figure 9D	Fraction of place or cue cells with >1 place field (by region)	One-way ANOVAs Place cells, $F_{(2,25)} = 0.04$; $p = 0.96$; Cue cells, $F_{(2,25)} = 2.653$; $p = 0.09$
Figure 9E	Peak trial-averaged, non-normalized activity (by region and cell type)	Two-way repeated–measure ANOVA Interaction of cell type and region, $F_{(2,25)} = 5.470$; $p = 0.0107$; Dunn–Šidák test, cue cells in RSC and M1, $t_{(50)} = 2.881$; $p = 0.017$; Main effect of cell type: $F_{(1,25)} = 51.37$; Dunn–Šidák test, RSC, $t_{(25)} = 1.298$; $p = 0.50$; M2, $t_{(25)} = 5.443$; $p < 0.0001$; M1, $t_{(25)} = 5.996$; $p < 0.0001$; No main effect of region: $F_{(2,25)} = 1.039$; $p = 0.37$
Figure 10A	Fraction of cue cells at obstacle locations (by region and lesion)	Two-way ANOVA No main effect of lesion: $F_{(2,41)} = 2.405$; $p = 0.10$; Main effect of region: $F_{(2,41)} = 20.94$; $p < 0.0001$; Presurgery: Tukey's test, RSC and M2, $p = 0.0007$; RSC and M1, $p < 0.0001$; M2 and M1, $p = 0.0083$; Sham: Tukey's test, RSC and M2, $p = 0.0468$; RSC and M1, $p = 0.0011$; M2 and M1, $p = 0.15$; Lesion: Tukey's test, RSC and M2, $p = 0.84$; RSC and M1, $p = 0.14$; M2 and M1, $p = 0.34$
Figure 10B	Spatial information (by lesion and cell type)	Two-way repeated–measure ANOVA Interaction in RSC: $F_{(2,11)} = 5.56$; $p = 0.0214$; Dunn–Šidák test, cue cells of sham and lesion, $t_{(22)} = 2.823$; $p = 0.029$; cue cells of presurgery and lesion, $t_{(22)} = 2.864$; $p = 0.027$; No main effect of lesion: RSC, $F_{(2,11)} = 2.326$; $p = 0.14$, M2: $F_{(2,17)} = 0.4551$; $p = 0.64$, M1: $F_{(2,13)} = 0.6364$; $p = 0.54$; Main effect of cell type: RSC, $F_{(1,11)} = 0.5465$; $p = 0.48$; M2, $F_{(1,17)} = 5.862$; $p = 0.027$; M1, $F_{(1,13)} = 103.0$; $p < 0.0001$
Figure 10C	Lifetime sparsity (by lesion and cell type)	Two-way repeated–measure ANOVA No main effect of lesion: RSC, $F_{(2,11)} = 1.807$; $p = 0.21$; M2, $F_{(2,17)} = 0.2731$; $p = 0.76$; M1, $F_{(2,13)} = 0.3039$; $p = 0.74$; Main effect of cell type: RSC, $F_{(1,11)} = 0.0496$; $p = 0.83$; M2, $F_{(1,17)} = 9.556$; $p = 0.0066$; M1, $F_{(1,13)} = 113.6$; $p < 0.0001$
Figure 10D	Fraction of place or cue cells with >1 place field (by lesion and cell type)	Two-way repeated–measure ANOVA No main effect of lesion: RSC, $F_{(2,11)} = 1.153$; $p = 0.35$; M2, $F_{(2,17)} = 1.394$; $p = 0.28$; M1, $F_{(2,13)} = 1.393$; $p = 0.28$; No main effect of cell type: RSC, $F_{(1,11)} = 2.369$; $p = 0.15$; M2, $F_{(1,17)} = 1.854$; $p = 0.19$; M1, $F_{(1,13)} = 0.0042$; $p = 0.95$
Figure 10E	Mean, non-normalized population activity	Coefficient of variation (SD/M) RSC: sham, 9.40%; lesion, 27.20%; M2, sham, 18.67%; lesion, 26.94%; M1, sham, 19.04%; lesion, 27.44%
Figure 10F	Non-normalized peak activity (by lesion and cell type)	Two-way repeated–measure ANOVA Interaction of lesion and cell type in RSC, $F_{(2,11)} = 10.94$; $p = 0.0024$; Dunn–Šidák test, sham and lesion, cue, $t_{(22)} = 2.715$; $p = 0.0375$; place, $t_{(22)} = 0.3924$; $p = 0.97$; Main effect of cell type: RSC, $F_{(1,11)} = 25.96$; $p = 0.0003$; M2, $F_{(1,17)} = 36.68$; $p < 0.0001$; M1, $F_{(1,13)} = 0.39.64$; $p < 0.0001$; No main effect of lesion: RSC, $F_{(2,11)} = 1.518$; $p = 0.26$; M2, $F_{(2,17)} = 0.1664$; $p = 0.85$; M1, $F_{(2,13)} = 0.1404$; $p = 0.87$
Figure 11A	Fractions of detected cells (by laminar division and lesion)	Two-way repeated–measure ANOVA Main effect of depth, $F_{(1.565,15.65)} = 17.09$; $p = 0.0002$; Tukey's test, upper and lower superficial, $p = 0.65$; upper superficial and deep: $p = 0.0068$, lower superficial and deep, $p < 0.0001$ No effect of lesion, $F_{(1,10)} = 2.542$; $p = 0.14$
Figure 11B	Fractions of position-correlated cells (by laminar division and lesion)	Two-way repeated–measure ANOVA Interaction of depth and lesion: $F_{(2,22)} = 12.14$; $p = 0.0003$; Sham: Dunn–Šidák test, upper and lower superficial, $t_{(6)} = 8.883$; $p = 0.0003$; upper superficial and deep, $t_{(6)} = 6.571$; $p = 0.0018$; lower superficial and deep, $t_{(6)} = 1.615$; $p = 0.40$; Lesion: Dunn–Šidák test, upper and lower superficial, $t_{(5)} = 0.1010$; $p = 1$; upper superficial and deep, $t_{(5)} = 1.355$, $p = 0.55$; lower superficial and deep, $t_{(5)} = 1.831$; $p = 0.33$
Figure 11C	Fractions of cue cells (by laminar division and lesion)	Two-way repeated–measure ANOVA No interaction of depth and lesion: $F_{(2,22)} = 0.9884$; $p = 0.39$; Sham: Dunn–Šidák test, upper and lower superficial, $t_{(6)} = 3.040$; $p = 0.067$; upper superficial and deep, $t_{(6)} = 63.645$; $p = 0.032$; lower superficial and deep, $t_{(6)} = 0.9835$; $p = 0.74$; Lesion: Dunn–Šidák test, upper and lower superficial, $t_{(5)} = 0.3376$; $p = 98$; upper superficial and deep, $t_{(5)} = 0.2987$; $p = 0.99$; lower superficial and deep, $t_{(5)} = 2,148$; $p = 1$
Figure 11D	Spatial information (by laminar division)	Two-sample Kolmogorov–Smirnov tests and Bonferroni-corrected $a = 0.008$ Sham: upper and lower superficial, $p < 0.0001$; upper superficial and deep, $p < 0.0001$; lower superficial and deep, $p = 0.0012$; Lesion: upper and lower superficial, p; upper superficial and deep, $p = 0.0002$; lower superficial and deep, $p = 0.048$

Table 1. Continued

| Figure	Variable	Statistical test(s) and results
Figure 11E	Lifetime sparsity (by laminar division)	Two-sample Kolmogorov–Smirnov tests and Bonferroni-corrected $a = 0.008$ Sham: upper and lower superficial, $p < 0.0001$; upper superficial and deep, $p < 0.0001$; lower superficial and deep, $p < 0.0001$; Lesion: upper and lower superficial, $p < 0.0001$; upper superficial and deep, $p < 0.0001$; lower superficial and deep, $p = 0.033$
Figure 11F	Mean, non-normalized population activity	Coefficient of variation (SD/M) Sham: upper superficial, 21.11%; lower superficial, 18.60%; deep, 14.61%; Lesion: upper superficial, 36.54%; lower superficial, 26.95%; deep, 31.92%
Figure 11G	Non-normalized peak activity (by lesion and depth)	Two-way repeated–measure ANOVA Main effect of depth: $F_{(1.414,12,72)} = 13.74$; $p = 0.0014$; Sham: Tukey's test, upper and lower superficial, $p = 0.0099$; upper superficial and deep, $p = 0.0037$; lower superficial and deep, $p = 0.037$; Lesion: Tukey's test, upper and lower superficial, $p = 0.46$; upper superficial and deep: $p = 0.36$; lower superficial and deep, $p = 0.27$; No main effect of lesion: $F_{(1,9)} = 0.3785$; $p = 0.55$
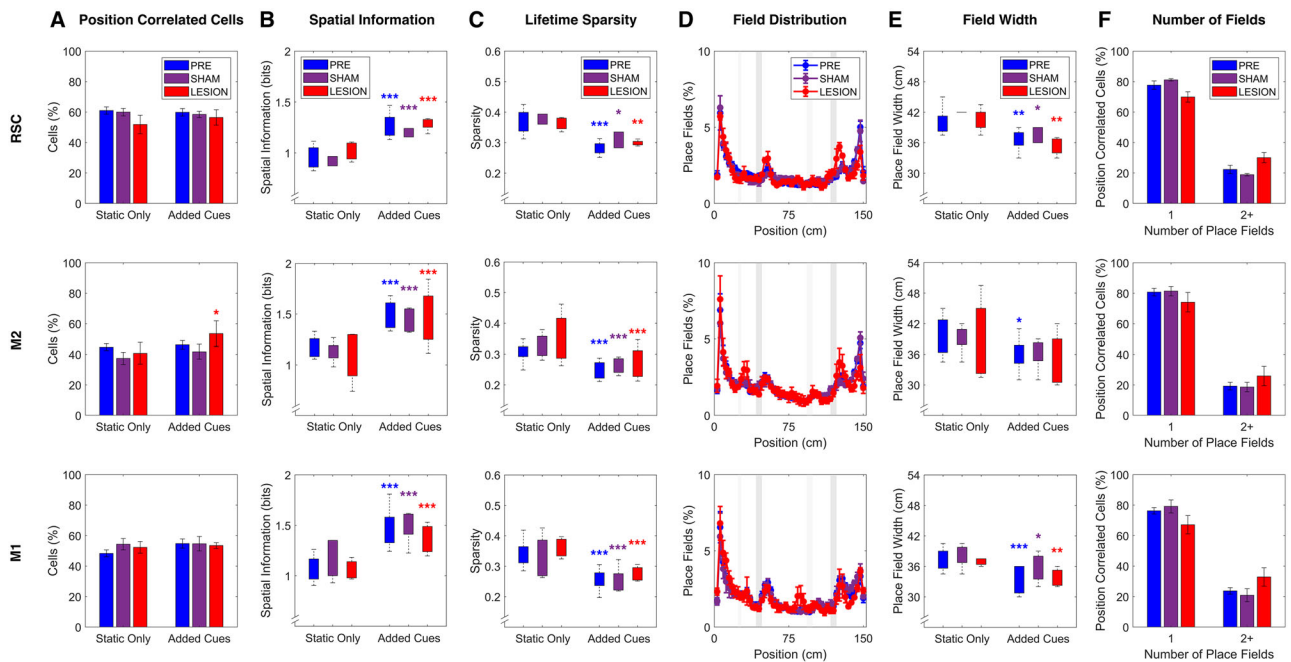
Figure 4. Position-correlated cortical cell characteristics were stable before and after bilateral sham or dorsal hippocampal lesions. *A*, Proportions of detected cells that were classified as position-correlated during sessions with static cues only or with the added obstacles. Error bars are SEM across mice. *B*, Median spatial information encoded by position-correlated cells during sessions with static cues only or with the added obstacles. For all boxplots, line, median; box, 25th and 75th percentiles; whiskers, minimum and maximum values; + signs, outliers. *C*, Lifetime sparsity of position-correlated cells during sessions with static cues only or with the added obstacles. *D*, Distributions of place field locations across the length of the treadmill belt. Gray bars indicate positions of stable cues (light gray) and interchangeable obstacles (dark gray). Error bars are SEM across mice. *E*, Median place field width of position-correlated cells during sessions with static cues only or with the added obstacles. *F*, Fractions of position-correlated cells exhibiting one or more (2+) place fields. Error bars are SEM across mice. Refer to Table 1 for summary of statistics.

Position-correlated sequences include both place- and cue-tuned cells

A common criticism of studies that employ head-fixed behavior is that position-correlated activity might be better explained by local sensory cues (including somatosensory, visual, or odor landmarks) and/or behavioral variables (such as motor patterns, rewards, or velocity) that were unaccounted for during analyses. Thus, to limit the influence of these variables and discern the distinct contributions of global location and sensorimotor information among position-correlated cells, analyses were next restricted to the locations of the two added, interchangeable obstacles. These locations were demarcated by the leading boundary of each obstacle and the area trailing those obstacles

that exhibited elevated fractions of place fields relative to days with static cues only (Fig. 7A). Consistent with the presence of cue-tuned cells within the larger position-correlated cell population, many of the place fields within these boundaries changed locations with the interchangeable obstacles (Fig. 7B). Furthermore, the length of these segments also roughly corresponded to the mean length of a mouse (15 cm; Fig. 7C), supporting that tactile sensation of the obstacles contributed to position-correlated coding within these regions of the environment. Nevertheless, a substantial fraction of place fields remained fixed to single locations. Thus, cue cells were defined as position-correlated cells that exhibited maximum mean normalized activity at the position of one specific obstacle, regardless of its
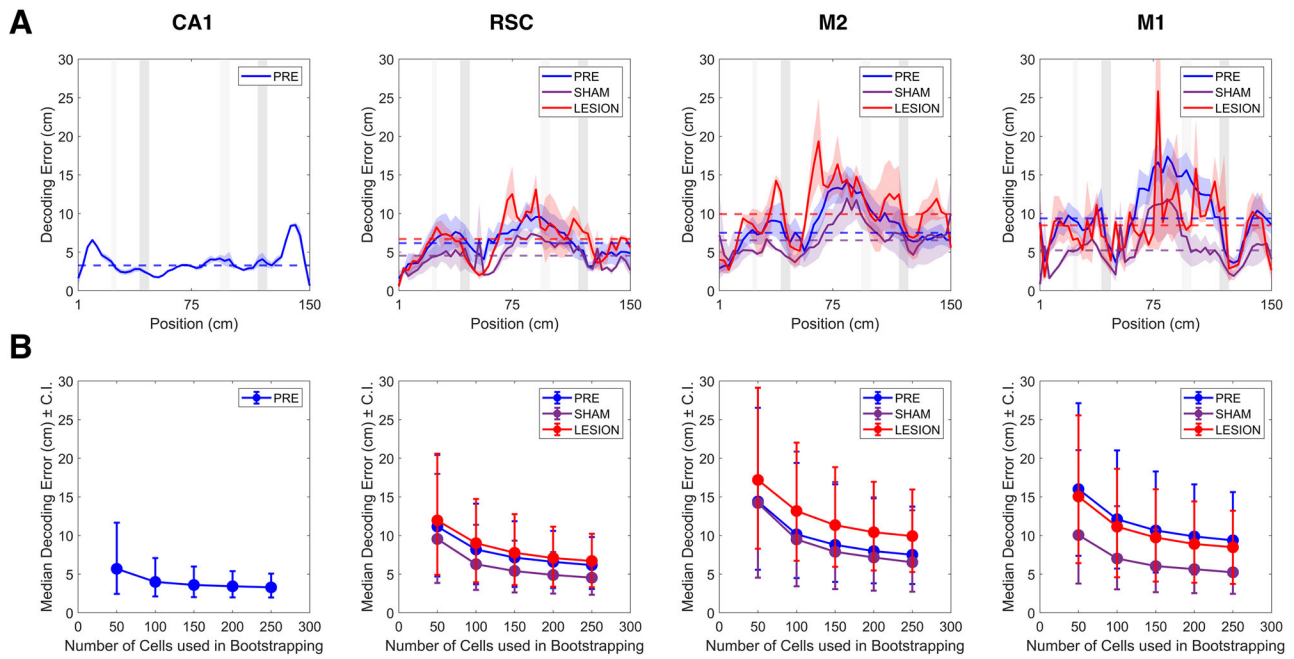
Figure 5. Bayesian decoding accuracy was not impaired by bilateral dorsal hippocampal lesions during traversal of a familiar environment. *A*, Mean Bayesian decoding error as a function of position along the binned length of the treadmill belt. Median is indicated by a dotted line for each lesion group. Gray bars indicate positions of stable cues (light gray) and interchangeable obstacles (dark gray). Shaded area is SEM across mice. *B*, Median decoding error as a function of the number of neurons used for bootstrapping. Dots indicate the median and error bars indicate the 95% confidence interval (CI). Note that, for all regions, median decoding error approximately plateaued at $M = 250$ neurons. Refer to Table 1 for summary of statistics.
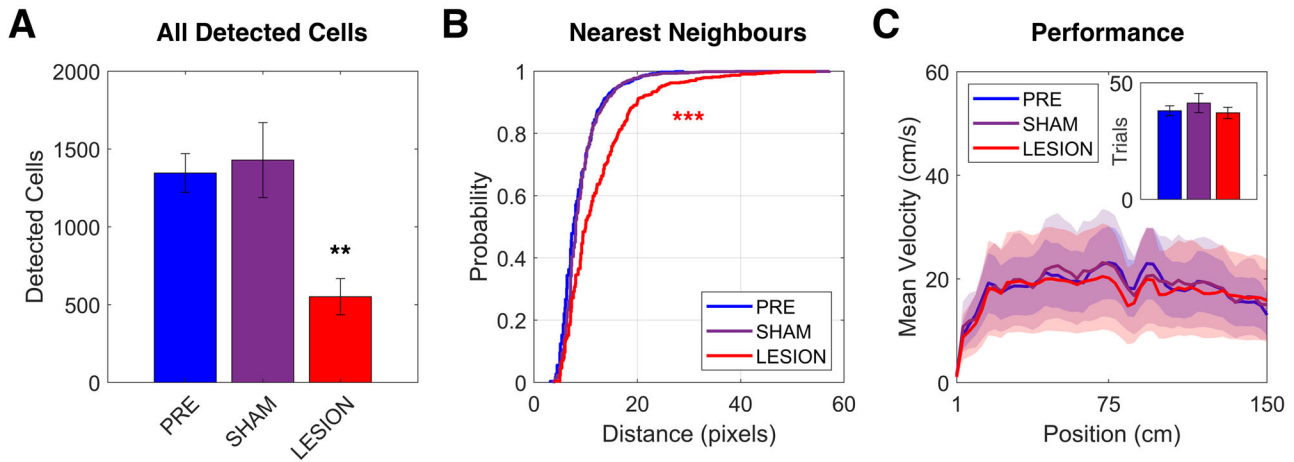

Figure 6. Fewer active cells were detected after bilateral dorsal hippocampal lesions. *A*, Mean number of total active cells detected across mice in each experimental treatment group. Error bars are SEM across mice. *B*, Cumulative distributions of distances between detected cells and their three nearest neighbors in each experimental treatment group. *C*, Mean velocity per trial (cm/s) as a function of position. Shaded area is SEM across mice. Note that mean velocity was not the same at the start and end of each trial because a brake was applied during the 15 s intertrial interval, during which time the velocity declined to 0 cm/s. The inset shows the mean number of laps run per ∼20 min experimental session. Error bars are SEM across mice. Refer to Table 1 for summary of statistics.

location on the track, whereas place cells were defined as position-correlated cells that always exhibited maximum mean normalized activity at the same location on the track, regardless of which obstacle was present (Fig. 7D).

Across all examined regions, the total population of position-correlated cells with fields at the interchangeable obstacle locations was composed of subpopulations of both place- and cue-tuned cells (Fig. 8A). Interestingly, both place and cue cells with either single or multiple fields often exhibited activity modulation by both of the interchangeable obstacles (Fig. 8B). For place cells, non-normalized peak activity was typically higher when one specific obstacle was positioned within the place

field, and, on average, these cells exhibited a ∼15–20% reduction in peak activity when the "nonpreferred" obstacle was moved into the place field. In contrast, the cue cell population was not modulated by obstacle location as there was no significant difference between the mean non-normalized peak activity at the preferred obstacle while it was positioned at either location. In addition, both cue and place cells with single fields demonstrated significantly elevated mean non-normalized activity at the nonpreferred obstacle or obstacle location, respectively, relative to the baseline (averaged across all treadmill locations that were at least 30 cm from the interchangeable obstacle locations). Altogether, these findings suggest that position-correlated cells
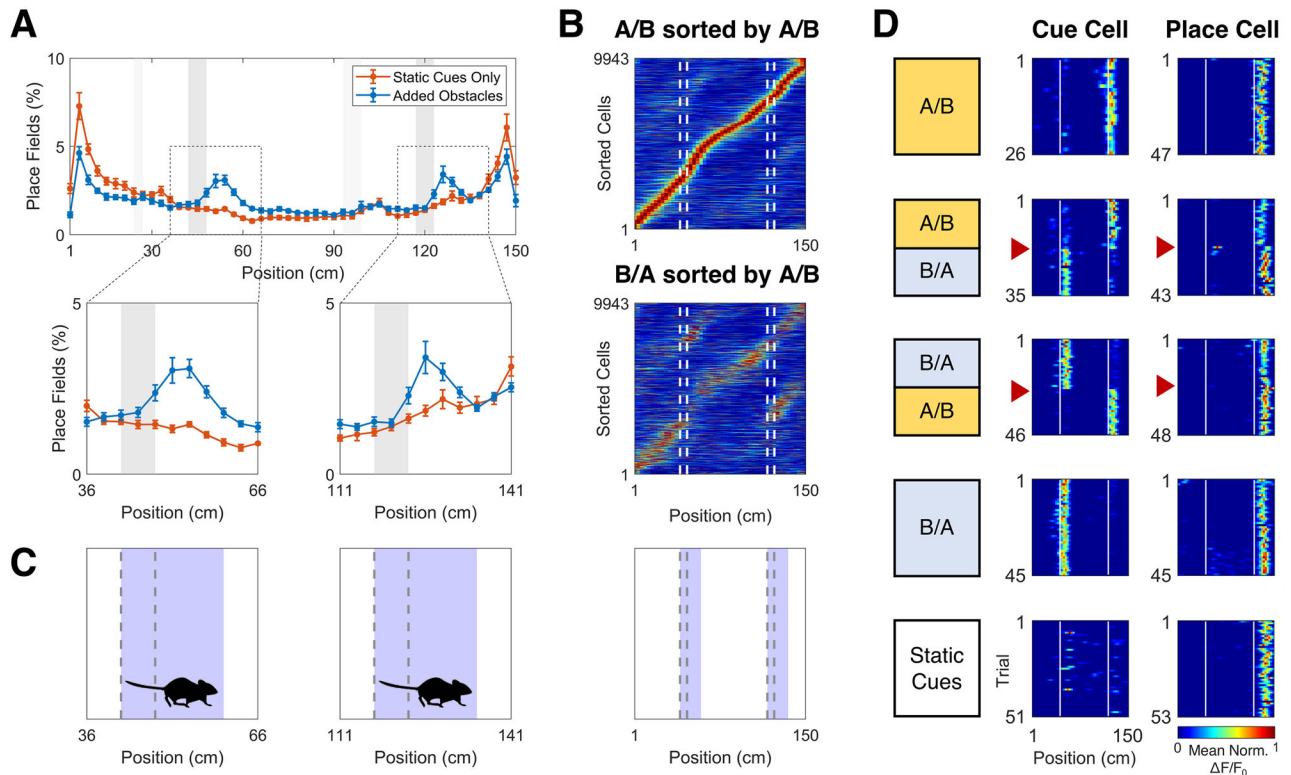
Figure 7. Criteria for the classification of position-correlated cells as place- or cue-tuned at the interchangeable obstacle locations. *A*, Top, Binned distributions of place field locations detected across RSC, M2, and M1 spanning the length of the treadmill belt and averaged across days with static cues only (orange) and days with added obstacles (blue). Error bars are SEM across mice. Gray bars indicate positions of stable cues (light gray) and interchangeable obstacles (dark gray). The outsets highlight an increased representation of fields trailing the obstacle locations (position A on left and position B on right). Note that the position of the forelimb is one bin (3 cm) delayed from where imaging occurs. *B*, Position-correlated cells were pooled across M2 of all presurgery mice on a cue-swap day. Top, Position-correlated cells were sorted by the order of maximum mean normalized $\Delta F/F_0$ during trials with obstacles in the A/B position. Bottom, Maximum mean normalized $\Delta F/F_0$ during trials with obstacles in the B/A position sorted by the order of maximum mean normalized $\Delta F/F_0$ during trials with obstacles in the A/B position (top). White dashed lines indicate the edges of the interchangeable obstacles. *C*, The regions of the environment (blue) that were analyzed for activity relating to the interchangeable obstacles for cue and place cell classification, which corresponded to (*A*) the locations of increased place fields after the obstacles were added, (*B*) place field movement during the cue-swaps, and the mean length of a mouse. The edges of the interchangeable obstacles are indicated by gray dashed lines. *D*, Representative cue cell and place cell from M2. Mean, normalized $\Delta F/F_0$ across laps on example days with the interchangeable obstacles in a stable configuration (A/B or B/A), on cue-swap days (A/B → B/A or B/A → A/B), and a day without the added interchangeable obstacles (Static Cues). White lines indicate the center positions of the interchangeable obstacles, and red arrows indicate the cue-swap trial.

in the neocortex undergo firing rate remapping to convey changing sensory information (Leutgeb et al., 2005; Allen et al., 2012; Navratilova et al., 2012), at least at locations in the environment where those cues demonstrate a salient relationship with each other.

Cortical representations exhibit reciprocal, interareal gradients of place and cue cells

Considering that any given environment may be represented by an amalgamation of cells that encode place, sensory cues, or other behavioral variables, general analysis of the entire population of position-correlated cells (with fields throughout the treadmill environment; Figs. 3, 4) could plausibly obscure any regional differences in one of these variables. Thus, the unique characteristics of the place and cue cell subpopulations (with fields at the interchangeable obstacle locations) were individually assessed. Interestingly, there were significantly different fractions of cue- and place-tuned cells across cortical regions in presurgery animals such that M1 exhibited significantly higher proportions of cue cells —and, conversely, fewer place cells—relative to M2 and RSC (Fig. 9A). In turn, the fraction of cue cells was also significantly higher in M2 relative to RSC, which did not significantly differ from hippocampal CA1 in the relative fractions of place and cue cells (data not shown; refer to Table 1 for summary of statistics).

Thus, for the regions studied, the proportions of detected place- and cue-tuned cells formed interareal gradients such that higher-level cortical regions exhibited larger fractions of place cells, similar to hippocampal CA1, whereas regions that were lower in the cortical hierarchy exhibited larger fractions of cue cells.

Despite differences in relative proportions, place cells at the interchangeable obstacle locations exhibited spatial characteristics that were comparable across cortical regions. There were no significant differences in encoded spatial information (Fig. 9B), lifetime sparsity (Fig. 9C), the number of cells that exhibited multiple place fields (Fig. 9D), or non-normalized peak activity (Fig. 9E). Notably, place cells in all regions exhibited ramping activity ahead of the obstacle locations, which was initiated around the location of the preceding static cue (Fig. 9E). In contrast, cue cells exhibited characteristics that varied consistently across the cortical hierarchy. Compared with cue cells in motor cortices, cue cells in RSC exhibited significantly lower spatial information (Fig. 9B) and higher measures of sparsity (Fig. 9C) and were more likely to exhibit multiple place fields (Fig. 9D). Consistent with increased spatial information among cue cells of M2 and M1, the trial-averaged, non-normalized peak activity of cue cells was significantly higher in these regions relative to RSC. In contrast, there was no difference between the peak activity of cue- and place-tuned cells in RSC, though only
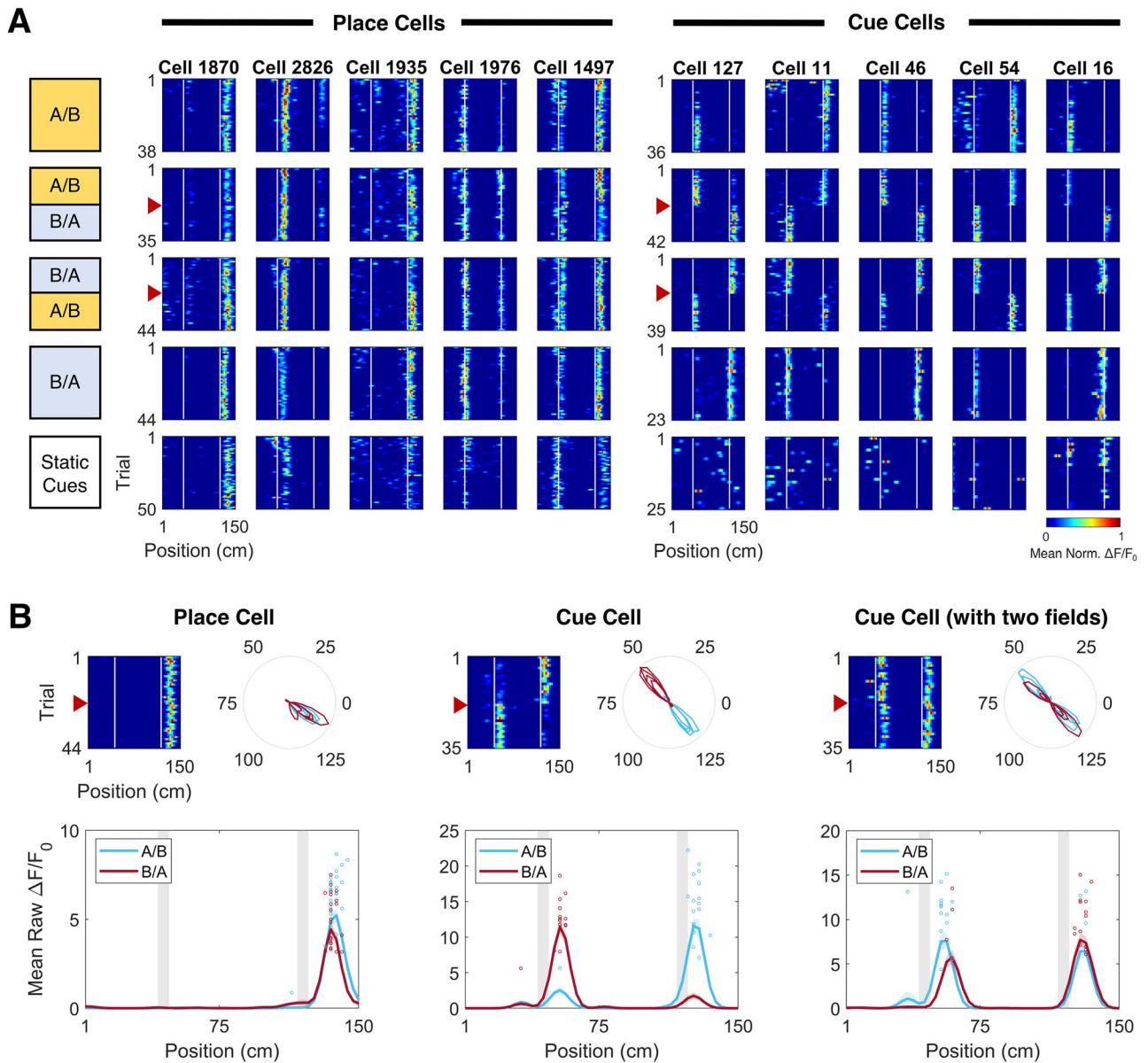
Figure 8. Representative place cells and cue cells. **A**, Mean, normalized $\Delta F/F_0$ across trials for example place and cue cells from one subject on days with the interchangeable obstacles in a stable configuration (A/B or B/A), on cue-swap days (A/B → B/A or B/A → A/B), and a day without the added interchangeable obstacles (Static Cues). White lines indicate the center positions of the interchangeable obstacles and red arrows indicate the cue-swap trial. **B**, Comparison of peak activity before and after the cue-swap among representative place and cue cells. Top left of each panel, Normalized mean $\Delta F/F_0$ across laps of an example cue-swap day where the obstacles changed orientations (A/B → B/A) midway through the session. White lines indicate positions of interchangeable obstacles and red arrows indicate the cue-swap. Top right of each panel, Polar plots showing trial-averaged, non-normalized $\Delta F/F_0$ for all cue-swap days (Days 4–7). Bottom panels, Trial-averaged, non-normalized mean $\Delta F/F_0$ as a function of position for the cells on an example cue-swap day where the obstacles changed orientations (A/B → B/A) midway through the session. Open circles indicate peak activity for each trial within the session. Gray bars indicate positions of interchangeable obstacles. Refer to Table 1 for summary of statistics.

place cells exhibited ramping activity (Fig. 9E). These findings support that cue cells in lower cortices augment spatial localization—encoding higher spatial information than place cells in all regions and cue cells in RSC—whereas place cells are highly uniform in their representation of space throughout the cortex and exhibit predictive activities.

Position-correlated cells in RSC exhibit increased cue-tuning after hippocampal lesions

The interareal gradients of place and cue cells may reflect the relative strength of descending contextual information (from the hippocampus) and ascending sensory inputs (from the thalamus). To test this assumption, we reexamined the place and

cue cell characteristics in mice after bilateral dorsal hippocampal lesions (i.e., after disruption of higher-level descending feedback). As observed among presurgery controls (Fig. 9A), RSC of sham controls exhibited significantly lower proportions of cue cells relative to M2 and M1. However, after bilateral lesions of the dorsal hippocampus, this effect was abolished, and RSC tended to exhibit higher fractions of cue-tuned cells (Fig. 10A). In addition, cue cells in RSC of lesioned mice encoded significantly higher spatial information (and trended toward lower lifetime sparsity indices) relative to cue-tuned cells of both presurgery and sham controls (Fig. 10B,C). This effect was not due to any differences across groups in the number of fields per cell (Fig. 10D) but, rather, was consistent with substantially
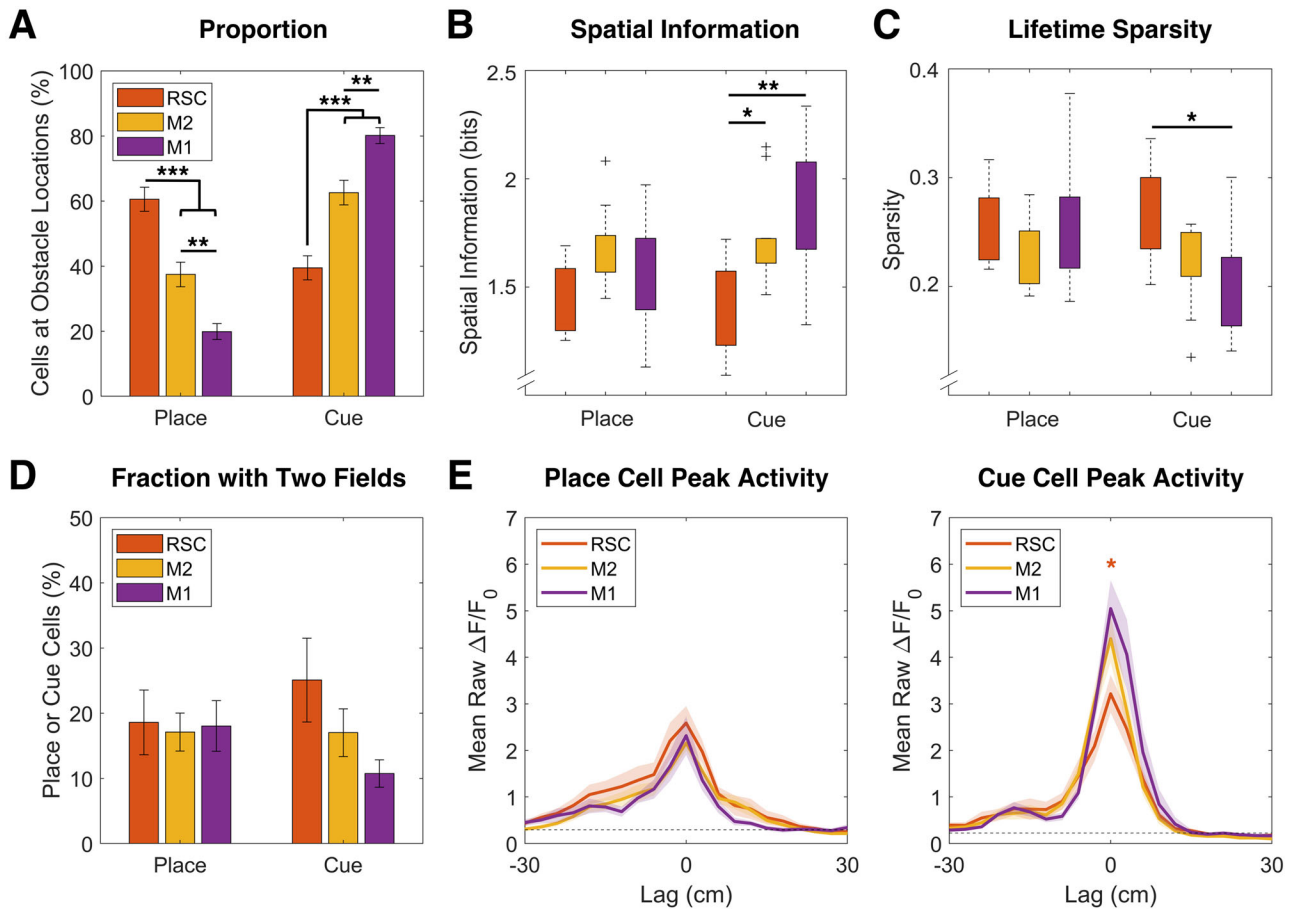
Figure 9. Lower-level cortices exhibited elevated fractions of cue cells with higher spatial information. *A*, Mean proportions of place- versus cue-tuned cells at the locations of the interchangeable obstacles in RSC (orange), M2 (yellow), and M1 (purple) of presurgery mice. Error bars are SEM across mice. *B*, Median spatial information encoded by place versus cue cells. For all boxplots, line, median; box, 25th and 75th percentiles; whiskers, minimum and maximum values; + signs, outliers. *C*, Median lifetime sparsity indices for place versus cue cells. *D*, Mean fractions of total place or cue cells that exhibited multiple place fields. Error bars are SEM across mice. *E*, Aligned peak non-normalized $\Delta F/F_0$ of place cells (left) and cue cells (right) with maximum mean normalized $\Delta F/F_0$ at one of the interchangeable obstacle locations. The shaded area is SEM across mice. Refer to Table 1 for summary of statistics.

elevated non-normalized population activity at the interchangeable obstacle locations after hippocampal lesions (Fig. 10E), which was at least partially a consequence of increased peak activity of cue cells with single fields (Fig. 10F). Although a spatial representation of the familiar environment persisted in all examined cortical regions, bilateral lesions of the dorsal hippocampus abolished the ramping activity of place cells (Fig. 10F) and disrupted the uniformity of the learned spatial representations at the locations of the interchangeable obstacles (Fig. 10G). Thus, an intact hippocampus appears to be necessary for the suppression of sensory-evoked responses in RSC and the online anticipation of spatial landmarks during active navigation.

Unlike RSC, there were no significant effects of hippocampal lesions on the fractions of cue- and place-tuned cells in M2 or M1 relative to presurgery (Fig. 9A) or sham controls (Fig. 10A). Among both place and cue cells of motor cortices, there were also no effects of lesion on encoded spatial information (Fig. 10B), lifetime sparsity (Fig. 10C), or the fractions of cells exhibiting multiple place fields (Fig. 10D). Nevertheless, non-normalized population activity was moderately elevated at the interchangeable obstacle locations after bilateral lesions of the dorsal hippocampus (refer to Fig. 10E), which—in contrast to RSC—was not a consequence of increased peak activity at the preferred firing locations of place or cue cells with single fields (Fig. 10F). Instead, this less-pronounced change in population

activity at the obstacle locations may be attributable to greater spatial clustering of activity (i.e., reduced uniformity of the spatial representation) or an obscured effect within a subpopulation of these cells (e.g., deep layer cells). In sum, whereas loss of an intact hippocampus directly augmented the relative contribution of sensorimotor variables to the representation of a familiar environment in RSC, this effect abated in downstream cortices.

Motor cortical volumes exhibit a laminar gradient of spatial information

The propagation of information flow throughout the cortex relies on stereotyped interareal and translaminar circuitry. In general, the perisomatic basal dendrites of excitatory neurons in L3 receive the majority of feedforward sensory inputs from lower cortices or thalamic areas via L4, whereas the distal apical dendrites of L2/3 and L5a neurons receive feedback inputs from higher-level cortical and thalamic areas via synaptic connections in L1 (Cauller and Connors, 1994; Petreanu et al., 2009; Sermet et al., 2019). Thus, it was hypothesized that there would also be distinct laminar patterns of spatial or sensorimotor tuning based on cell depth. Although laminar analyses were not possible in dysgranular RSC due to the anterior medial location of imaging (Allen Brain Institute for Science, 2011), two-photon imaging extended from ~170 to 485 μm below the pial surface in the motor cortex, enabling quantification of the depth-dependent
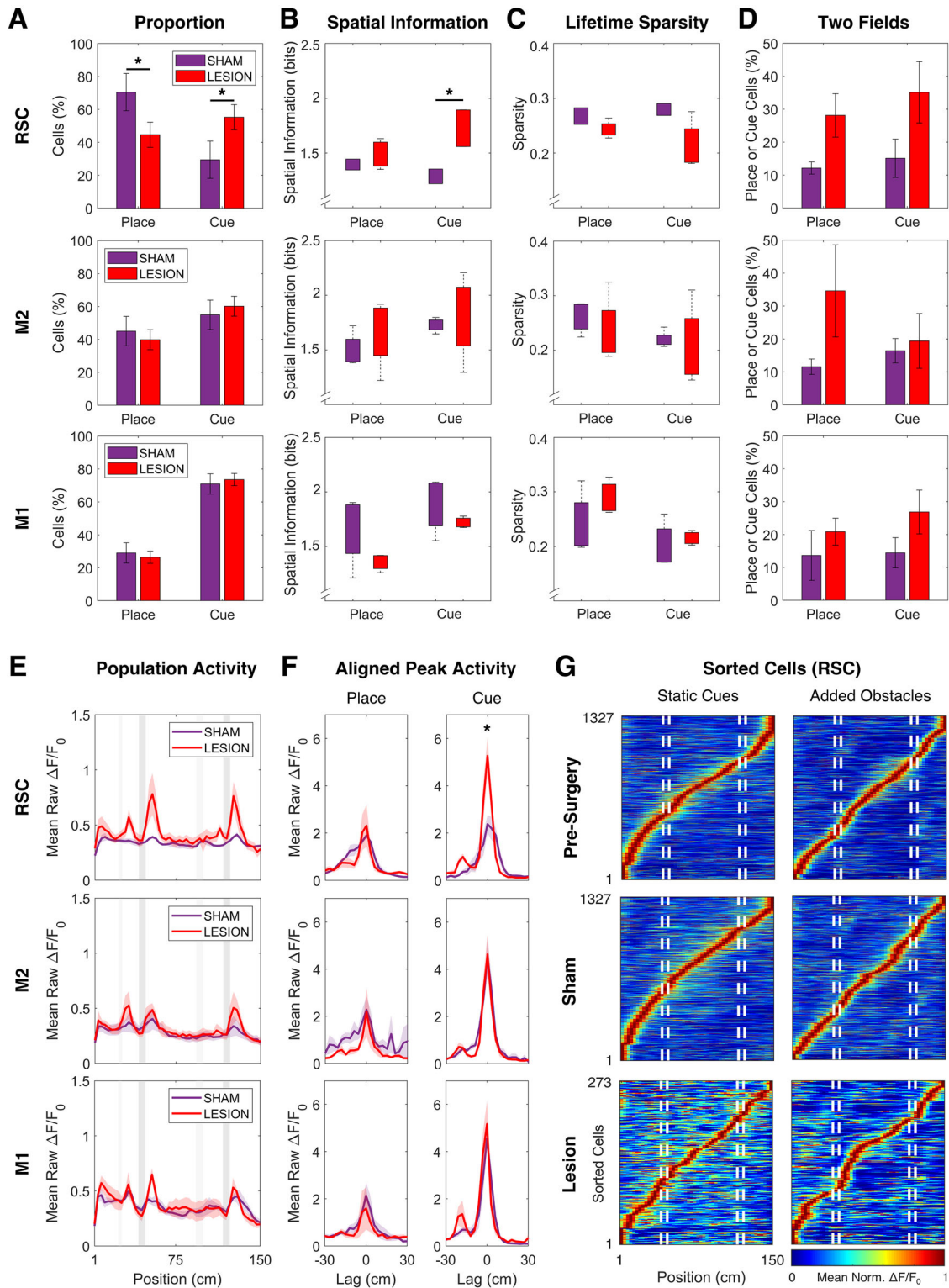
Figure 10. After bilateral lesions of the dorsal hippocampus, RSC exhibited increased cue-tuning, analogous to motor cortices of control mice. **A**, Fractions of place and cue cells detected at the locations of the interchangeable obstacles in RSC, M2, and M1 of sham controls (purple) and hippocampus-lesioned mice (red). **B**, Median encoded spatial information and (**C**) median lifetime sparsity of place- and cue-tuned cells of mice with sham or bilateral lesions of the dorsal hippocampus. For all boxplots, box, 25th and 75th percentiles; whiskers, minimum and maximum values; + signs, outliers. **D**, Fractions of total place or cue cells detected at the interchangeable obstacle locations that exhibited two place fields on cue-swap days. Error bars are SEM across mice. **E**, Mean non-normalized $\Delta F/F_0$ of all detected cells after sham or bilateral lesions of the dorsal hippocampus. The shaded area is SEM across mice. Gray bars indicate positions of stable cues (light gray) and interchangeable obstacles (dark gray). **F**, Aligned peak non-normalized $\Delta F/F_0$ of place cells (left) and cue cells (right) with maximum mean normalized $\Delta F/F_0$ at one of the interchangeable obstacle locations. The shaded area is SEM across mice. Note the ramping activity of place cells in sham controls, which was initiated at the location of the preceding static cue, and its reduction after bilateral lesions of the dorsal hippocampus. **G**, Position-correlated cells from RSC of example mice were sorted by the order of maximum mean normalized $\Delta F/F_0$ on the last days before and the first days after sham or hippocampal lesion surgeries. Days with static cues only (left) correspond with Day 10 (presurgery) and Day 1 (postsurgery) of the 10 d paradigm, whereas days with added obstacles (right) correspond with Day 8 (presurgery) and Day 3 (postsurgery). White dashed lines indicate the boundaries of the interchangeable obstacles. Note the over-representation of the interchangeable cue locations after hippocampal lesions. Refer to Table 1 for summary of statistics.

characteristics of position-correlated cells in this region. Based on anatomical atlases (Allen Brain Institute for Science, 2011), the boundary between superficial (L2/3) and deep (L5a) layers was expected to be located at a depth of ~400 μm in the motor cortex. Corresponding with this approximation, the three z-planes below this division exhibited a higher density of active cells in any given experimental session relative to planes above 400 μm, which is also consistent with evidence of sparse and dense coding strategies in L2/3 and L5, respectively (for reviews, see Barth and Poulet, 2012; Petersen and Crochet, 2013). Superficial cells were further divided into "upper" and "lower" divisions such that cells from the most superficial three z-planes 1–3 were classified as upper L2/3 (upper superficial; ~170–240 μm below the pial surface) and cells from z-planes 4–6

were classified as lower L2/3 (lower superficial; ~275–345 μm below the pial surface). Cells detected in the deepest three z-planes 8–10 were classified as L5a (deep; ~415–485 μm below the pial surface), and the intermediate Plane 7 was excluded to account for variations in the location of the boundary between L2/3 and L5a across mice. When all detected cells were grouped by these laminar divisions, there were significantly fewer deep layer cells recorded across mice relative to upper and lower superficial cells (Fig. 11A), which was a consequence of two-photon imaging depth limitations that arise due to light scattering and the poor signal contrast of green-shifted fluorophores in deep layers.

The fractions of position-correlated cells detected in each z-plane formed a gradient that spanned the superficial layers
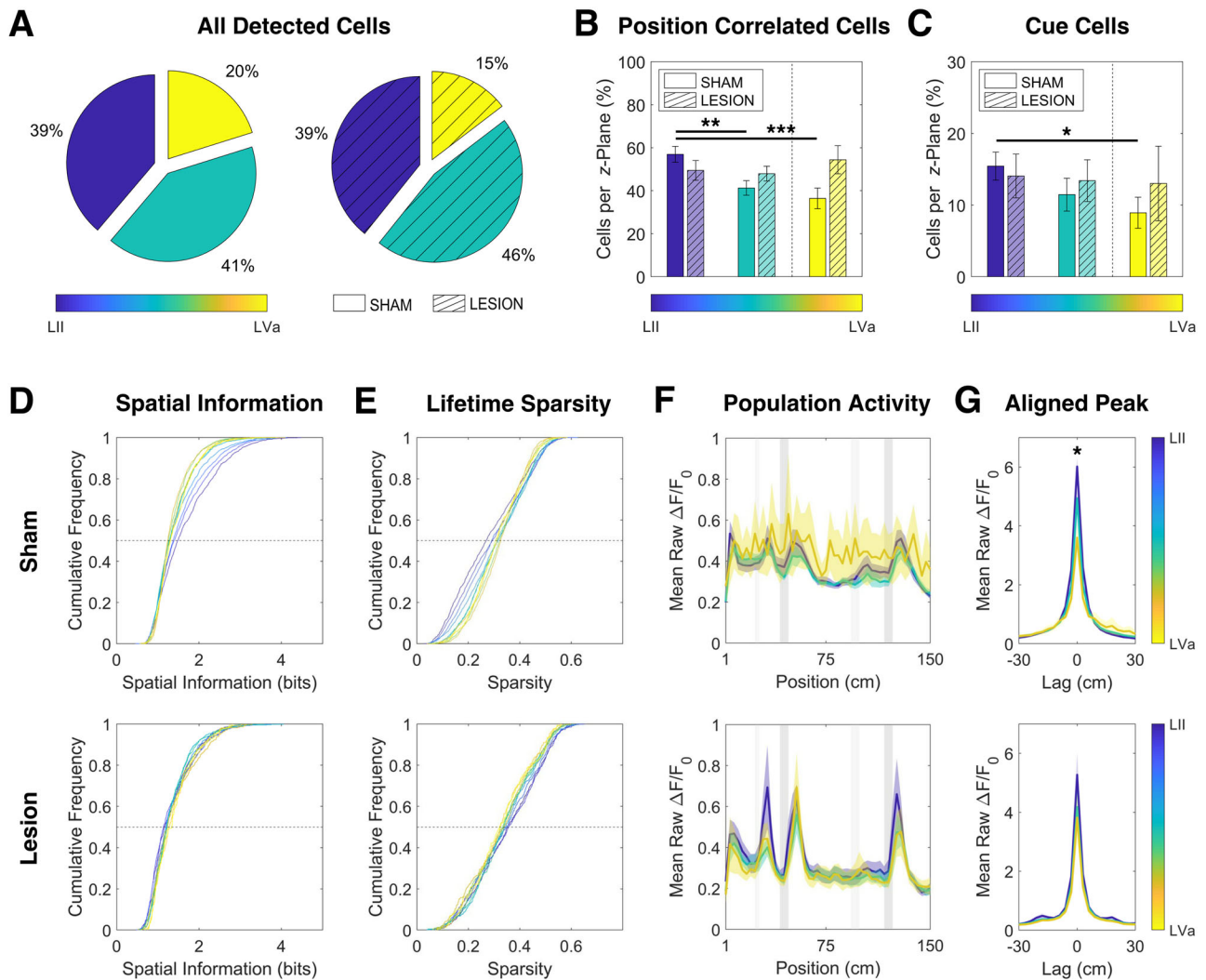

Figure 11. Spatial selectivity formed a translaminar gradient in the motor cortex that was abolished after bilateral dorsal hippocampal lesions. **A**, Mean fractions of all detected cells, grouped by cortical depth, in the motor cortex of sham controls and mice with bilateral lesions of the dorsal hippocampus. Superficial L2/3 cells were divided into upper (dark blue) and lower (teal) fractions, whereas deep L5a cells are shown separately (yellow). **B**, Proportion of all cells within each laminar subdivision that were classified as position-correlated at any location throughout the treadmill environment. **C**, Proportion of all cells within each laminar subdivision that were classified as cue-tuned at the interchangeable obstacle locations. Note the difference in scale between (**B**) and (**C**) and that cue-tuned cells also fit the criteria for position correlated and so are also represented in **B**. The fractions of place-tuned cells at the interchangeable obstacle locations were comparatively small in the motor cortex and so are not shown. For all plots, the dashed line indicates the approximate boundary between L3 and L5 (~400 μm below the cortical surface). Error bars are SEM across mice. **D**, Cumulative frequency distributions of spatial information encoded by neurons. Cells were pooled across mice for each treatment group. **E**, Cumulative frequency distributions of sparsity indices. Cells were pooled across mice for each treatment group. **F**, Trial-averaged, non-normalized ΔF/F₀, averaged across all detected neurons in upper superficial, lower superficial, and deep layers as a function of binned location on the treadmill. Shaded area is SEM across mice. Gray bars indicate the positions of the stable cues (light gray) and interchangeable obstacles (dark gray). **G**, Aligned peak non-normalized ΔF/F₀ of all upper superficial, lower superficial, and deep cells. The shaded area is SEM across mice. Refer to Table 1 for summary of statistics.

with the lowest proportions evident at or just below the boundary between L3 and L5. When compared by grouped laminar division, the fraction of all position-correlated cells detected in the upper superficial layer of sham controls was significantly higher than lower superficial and deep layers (Fig. 11B). Subsets of cue-tuned cells at the interchangeable obstacle locations were also evident throughout the depth of the cortex and similarly formed a gradient across the cortical volume that was roughly proportionate to the laminar distribution of all position-correlated cells (Fig. 11C). Consistent with elevated spatial selectivity in superficial layers, cells located in z-planes closer to the cortical surface encoded higher spatial information (Fig. 11D) and exhibited reduced lifetime sparsity indices (Fig. 11E). These measures each formed a gradient that extended into deep layers, with deep cells encoding the lowest spatial information and exhibiting the highest lifetime sparsity indices.

The distribution of population activity (averaged across all detected cells at each binned position on the treadmill) was also different across the cortical volume. Cell populations in more superficial imaging z-planes exhibited moderately elevated non-normalized activity trailing cued locations in the environment, a trend that was not evident in deep layers (Fig. 11F). Consistent with enhanced cue-tuning, the trial-averaged, non-normalized peak activity of position-correlated cells was significantly higher in upper superficial planes relative to lower superficial and deep planes and in lower superficial relative to deep planes (Fig. 11G). Altogether, cells that were located closer to the cortical surface were more likely to be position correlated and to exhibit higher cue modulation.

Position-correlated cell activity becomes homogeneous across layers after hippocampal lesions
Although the characteristics of place and cue cells in the motor cortex appeared to be relatively unaffected by dorsal hippocampal lesions (Fig. 10), a reduction in descending feedback might have specifically impacted deeper cells, an effect that would be masked by the significantly larger fraction of detected superficial cells (Fig. 11A). Thus, the translaminar distributions of position-correlated cells and their characteristics were reassessed after bilateral lesions of the dorsal hippocampus. Importantly, there was no effect of lesion on the relative fractions of total detected cells per grouped laminar division (Fig. 11A). However, the gradient of position-correlated cell recruitment was largely abolished such that the proportions of position-correlated cells (detected throughout the entire environment; Fig. 11B) and cue cells (at the interchangeable obstacle locations; Fig. 11C) increased in lower superficial and deep layers—particularly in upper L5a—of lesioned mice. Depth-dependent differences in encoded spatial information (Fig. 11D) and lifetime sparsity (Fig. 11E) were also reduced. In particular, spatial information increased among lower superficial and deep layer cells, a result that is consistent with increased cue-tuning in these layers. Moreover, the differences in mean population activity were also largely attenuated such that cells at all depths exhibited homogeneously elevated activation at the cued locations (Fig. 11F), and there were no longer significant differences between the trial-averaged, non-normalized peak activity of position-correlated cells in upper superficial, lower superficial, and deep planes (Fig. 11G). In sum, in the absence of an intact hippocampus, the recruitment and spatial characteristics of position-correlated cells were more uniform across the cortical depth relative to sham controls and, in general, cue-specific activity was enhanced across layers. These findings suggest that

hippocampal feedback propagates downstream and indirectly suppresses sensory-evoked activity around the boundary of L3/5 of the motor cortex, where pyramidal neurons exhibit the archetypal molecular markers and input–output circuits of L4 of other sensory cortices (Skoglund et al., 1997; Yamawaki et al., 2014; Bopp et al., 2017).

Discussion
This study discerned the relative encoding of spatial and sensorimotor information among position-correlated cells in RSC, M2, and M1 and assessed the continued influence of hippocampal modulation on the cortical representation of a familiar environment. Across this cortical hierarchy, reciprocal, interareal gradients of place- and cue-tuned cells jointly encoded the positions of two unstable obstacles such that higher-level cortices exhibited greater fractions of place-tuned cells, whereas lower-level regions exhibited greater fractions of cue-tuned cells. Although a cortical representation of the learned environment persisted after bilateral dorsal hippocampal lesions, there was a marked shift from place- to cue-tuning in RSC, and both the recruitment of position-correlated cells and their activity at the two unstable obstacle locations became homogeneously elevated across laminae in motor cortices. Taken together, the hippocampus appears to enduringly support the online binding of unreliable sensory attributes to a coherent contextual framework during navigation of a familiar environment. In turn, descending feedback modulates sensory-evoked cortical responses during ongoing behavior—an effect that is strongest in the adjacent RSC but propagates to lower cortices according to stereotyped laminar circuitry.

The abundance of place-tuned cells in RSC can likely be attributed to direct interconnectivity with the hippocampal formation (Vogt and Miller, 1983; van Groen and Wyss, 1992, 2003; Sugar et al., 2011). In the absence of spatiotemporal inputs from the hippocampus, increased cue-specific tuning in RSC may reflect a local imbalance between global contextual and local sensory inputs, with responses being principally driven by locomotor information and optic flow (Yamawaki et al., 2016; Mao et al., 2020). Moreover, the dorsal subiculum—which mediates the majority of the interactions between CA1 and dysgranular RSC—was also lesioned in this study. CA1-projecting subiculum cells modulate the responses of place cells to displaced objects (Sun et al., 2019) and may be crucial for tracking object location in allocentric space. Thus, even in familiar environments, the dorsal hippocampus and subiculum appear to remain essential for updating or stabilizing a global spatial representation amid unreliable sensory information.

In contrast to RSC, the balance of tuning among position-correlated cells in motor cortices was consistently biased toward the manipulated cues, likely because ascending sensory input predominates in these regions. Even after dorsal hippocampal lesions, peak activity and spatial information were augmented among cue-tuned cells in motor cortices, supporting that stimulus-evoked responses may largely overshadow top–down inputs in lower-level regions. Notably, there was also a marked overrepresentation of the unstable obstacles relative to the stable cues. This object instability may have enhanced the attentional state of the animals, increasing spatial resolution in the motor cortices at those locations (Kentros et al., 2004). Alternatively, or as an additional consequence of an attentive state (Alink and Blank, 2021), there may have been repetition or expectation suppression of responses to the predictable stable cues (Henson et al., 2000; Summerfield et al., 2008; Todorovic et al., 2011; Richter et al., 2018). Furthermore, hippocampal place cells tend

not to orient their place fields to unstable environmental cues (Knierim et al., 1995), and the RSC preferentially encodes permanent landmarks in humans (Auger et al., 2012, 2015) and behaviorally significant or context-identifying cues in rats (Smith et al., 2012; Vedder et al., 2017). Thus, increased activity at the unreliable cue locations in lower cortices may also reflect reduced top–down modulation and a greater reliance on local sensory inputs for driving appropriate behavioral responses.

Across layers of motor cortices, the distribution of position-correlated cells and their encoded spatial information formed a gradient such that superficial cells closer to the cortical surface were more likely to be position correlated and were more sparsely and precisely tuned than deeper cells. Previous studies in RSC (Mao et al., 2017) and S1 (Long and Zhang, 2021) have similarly reported low fractions of position-correlated cells in L5a. However, bilateral dorsal hippocampal lesions increased both recruitment and the spatial information of position-correlated cells within upper L5a, which coincides with the location of sensory thalamic inputs to the motor cortex (Hooks et al., 2013). Thus, in intact mice, descending hippocampal feedback appears to indirectly suppress the stimulus-evoked recruitment of position-correlated cells in the thalamic input layer of lower cortices while simultaneously enhancing spatial tuning among superficial cells during behavior in a familiar environment. Although resolving the local circuits that facilitate translaminar activity dynamics is beyond the scope of this study, both feedback projections to L1 and L2/3 output converge on L5, and the net effect of L5 activation is recurrent suppression of L2–4 (Onodera and Kato, 2022). Accordingly, learning has been shown to gradually enhance descending inputs from RSC to L1 while sparsening the activity of downstream L2–4 cells in V1 (Makino and Komiyama, 2015), and optogenetic stimulation of L5 in the auditory cortex sharpens frequency tuning and reduces the amplitude of tone-evoked responses in superficial layers (Onodera and Kato, 2022), analogous to the laminar effects of intact hippocampal input in the motor cortex.

Whereas the properties of cue cells were maintained after dorsal hippocampal lesions, the ramping activity of place cells (in anticipation of upcoming sensory cues) was abolished, a finding that validates other recent observations of predictive activities among cortical neurons. For instance, Lande et al. (2023) also identified a subpopulation of "trace cells" in RSC that maintained stable tuning at the position of a tactile cue after it was removed from a treadmill environment (i.e., place cells) and "nontrace cells" that lost tuning when the object was removed (i.e., cue cells). The trace cells—but not the nontrace cells—similarly exhibited ramping activity up to 50 cm in advance of contact with the objects. In another study, Makino and Komiyama (2015) observed that anticipatory activity emerged as a consequence of learning a visually guided active avoidance task. Both synaptic boutons from RSC and excitatory cells in superficial V1 were predominantly responsive to the visual stimulus onset in naive animals but, with learning, eventually exhibited ramping activity specific for the stimulus offset and the coincident timing of an aversive shock. Importantly, ramping was abolished after postlearning inactivation of the RSC, supporting that descending inputs from RSC modulate task-dependent responses in V1 (Makino and Komiyama, 2015). However, the results of the current study imply that these context-dependent signals originate in the hippocampus and are distributed to lower cortices via RSC. In any case, cortical cells of intact animals continue to receive top–down modulation that enables online prediction of salient stimuli in a familiar environment.

Considering that fewer active cells were detected in lesioned animals, a potential caveat is that the reported effects may be due to decreased recruitment in superficial layers or a detection bias toward highly active cells after a generalized decrease in firing rates. However, these explanations seem unlikely as the relative fractions of active cells detected across laminar divisions of sham and lesioned animals were not significantly different and encoded spatial information was selectively increased in deep layers of lesioned animals relative to controls. Moreover, as previously described, optogenetic manipulation of L5 (Onodera and Kato, 2022) and inactivation of RSC (Makino and Komiyama, 2015) have produced complementary results, suggesting that the lesion effects are more plausibly due to interruption of descending pathways rather than gross impairments. Finally, such a hippocampal effect on cell recruitment has not been reported by other lesion studies from our lab group (Mao et al., 2018; Esteves et al., 2021, 2023). A possible methodological limitation in the current study is that, whenever possible, cellular ROIs were registered across both presurgery and postsurgery days. However, cortical distortion necessitated independent registration of postsurgery reference frames in subjects with complete dorsal hippocampal lesions. Thus, in addition to uncontrolled variability in the clarity of the imaging frames across mice, the total number of cells detected in controls may have been inflated by ongoing representational drift over time (Ziv et al., 2013; Driscoll et al., 2017). To eliminate this variable, future studies should strive to quantify both inactive and active cells.

Taken together, this study provides evidence that the hierarchical regional and laminar organization of the cortex scaffolds the integration of descending contextual and ascending sensory inputs during navigation of a familiar environment. Although recall of remote contextual memories depends on RSC (Corcoran et al., 2011; Katche et al., 2013; Todd et al., 2016), which may assume the long-term role of storing allocentric spatial representations after hippocampus-dependent learning, the hippocampus appears to remain necessary for updating the internal model of the environment amid unreliable sensory information. Atop the cortical hierarchy in hippocampal CA3 —a subregion that maintains a spatial code that is robust against changes to environmental cues (Lee et al., 2004; Neunuebel and Knierim, 2014)—autoassociative pattern completion mechanisms may function to bind changing sensory attributes of experience to a stable contextual framework (Teyler and DiScenna, 1986; Rolls, 2013). In turn, top–down feedback can more effectively anticipate future behaviors and modify stimulus-evoked cortical responses that are congruent with the current internal model, perhaps through recruitment of a distributed cortical network that can locally modulate the balance between excitation and inhibition. Importantly, the results are consistent with descending suppression of ascending sensory-evoked responses, which substantiates a central hypothesis of the predictive coding theoretical framework (Srinivasan et al., 1982; Rao and Ballard, 1999; Friston, 2005). Therefore, the results lend support for a dual role of the hippocampus in both facilitating the coordinated reinstatement of distributed cortical memory representations and propagating top–down predictions to enhance the efficiency of information processing (Barron et al., 2020).

References

Alink A, Blank H (2021) Can expectation suppression be explained by reduced attention to predictable stimuli? Neuroimage 231:117824.

Allen K, Rawlins JNP, Bannerman DM, Csicsvari J (2012) Hippocampal place cells can encode multiple trial-dependent features through rate remapping. J Neurosci 32:14752–14766.

Allen Brain Institute for Science (2011) Allen reference atlas – mouse brain. atlas.brain-map.org.

Auger SD, Mullally SL, Maguire EA (2012) Retrosplenial cortex codes for permanent landmarks. PLoS One 7:e43620.

Auger SD, Zeidman P, Maguire EA (2015) A central role for the retrosplenial cortex in de novo environmental learning. eLife 4:e09031.

Bakker R, Tiesinga P, Kötter R (2015) The scalable brain atlas: instant web-based access to public brain atlases and related content. Neuroinformatics 13:353–366.

Barnes CA, McNaughton BL, Mizumori SJY, Leonard BW, Lin L-H (1990) Comparison of spatial and temporal characteristics of neuronal activity in sequential stages of hippocampal processing. Prog Brain Res 83:287–300.

Barron HC, Auksztulewicz R, Friston K (2020) Prediction and memory: a predictive coding account. Prog Neurobiol 192:101821.

Barth AL, Poulet JFA (2012) Experimental evidence for sparse firing in the neocortex. Trends Neurosci 35:345–355.

Bickel PJ, Sakov A (2008) On the choice of m in the m out of n bootstrap and confidence bounds for extrema. Stat Sin 18:967–985.

Bopp R, Holler-Rickauer S, Martin KAC, Schuhknecht GFP (2017) An ultrastructural study of the thalamic input to layer 4 of primary motor and primary somatosensory cortex in the mouse. J Neurosci 37:2435–2448.

Bourboulou R, Marti G, Michon F-X, El Feghaly E, Nouguier M, Robbe D, Koenig J, Epsztein J (2019) Dynamic control of hippocampal spatial coding resolution by local visual cues. eLife 8:e44487.

Brose N, Gasic GP, Vetter DE, Sullivan JM, Heinemann SF (1993) Protein chemical characterization and immunocytochemical localization of the NMDA receptor subunit NMDA R1. J Biol Chem 268:22663–22671.

Burke SN, Maurer AP, Nematollahi S, Uprety AR, Wallace JL, Barnes CA (2011) The influence of objects on place field expression and size in distal hippocampal CA1. Hippocampus 21:783–801.

Buzsáki G (1989) Two-stage model of memory trace formation: a role for "noisy" brain states. Neuroscience 31:551–570.

Cauller LJ, Connors BW (1994) Synaptic physiology of horizontal afferents to layer I in slices of rat SI neocortex. J Neurosci 14:751–762.

Chang HR, Esteves IM, Neumann AR, Sun J, Mohajerani MH, McNaughton BL (2020) Coordinated activities of retrosplenial ensembles during resting-state encode spatial landmarks. Philos Trans R Soc Lond B Biol Sci 375:20190228.

Climer JR, Dombeck DA (2021) Information theoretic approaches to deciphering the neural code with functional fluorescence imaging. eNeuro 8:ENEURO.0266-21.2021.

Corcoran KA, Donnan MD, Tronson NC, Guzmán YF, Gao C, Jovasevic V, Guedea AL, Radulovic J (2011) NMDA receptors in retrosplenial cortex are necessary for retrieval of recent and remote context fear memory. J Neurosci 31:11655.

Douglas RJ, Martin KAC (2004) Neuronal circuits of the neocortex. Annu Rev Neurosci 27:419–451.

Driscoll LN, Pettit NL, Minderer M, Chettih SN, Harvey CD (2017) Dynamic reorganization of neuronal activity patterns in parietal cortex. Cell 170:986–999.e16.

Esteves IM, Chang H, Neumann AR, McNaughton BL (2023) Consolidation of cellular memory representations in superficial neocortex. iScience 26:105970.

Esteves IM, Chang H, Neumann AR, Sun J, Mohajerani MH, McNaughton BL (2021) Spatial information encoding across multiple neocortical regions depends on an intact hippocampus. J Neurosci 41:307–319.

Euston DR, Tatsuno M, McNaughton BL (2007) Fast-forward playback of recent memory sequences in prefrontal cortex during sleep. Science 318:1147–1150.

Felleman DJ, Van Essen DC (1991) Distributed hierarchical processing in the primate cerebral cortex. Cereb Cortex 1:1–47. https://academic.oup.com/cercor/article/1/1/1/408896

Friston K (2005) A theory of cortical responses. Philos Trans R Soc Lond B Biol Sci 360:815–836.

Fujisawa S, Amarasingham A, Harrison MT, Buzsáki G (2008) Behavior-dependent short-term assembly dynamics in the medial prefrontal cortex. Nat Neurosci 11:823–833.

Gauthier JL, Tank DW (2018) A dedicated population for reward coding in the hippocampus. Neuron 99:179–193.e7.

Gianatti M, Garvert AC, Lenkey N, Ebbesen NC, Hennestad E, Vervaeke K (2023) Multiple long-range projections convey position information to the agranular retrosplenial cortex. Cell Rep 42:113109.

Gupta AS, van der Meer MAA, Touretzky DS, Redish AD (2010) Hippocampal replay is not a simple function of experience. Neuron 65:695–705.

Henson R, Shallice T, Dolan R (2000) Neuroimaging evidence for dissociable forms of repetition priming. Science 287:1269–1272.

Hollup SA, Molden S, Donnett JG, Moser M-B, Moser EI (2001) Accumulation of hippocampal place fields at the goal location in an annular watermaze task. J Neurosci 21:1635.

Hooks BM, Mao T, Gutnisky DA, Yamawaki N, Svoboda K, Shepherd GMG (2013) Organization of cortical and thalamic input to pyramidal neurons in mouse motor cortex. J Neurosci 33:748–760.

Inayat S, McAllister BB, Whishaw IQ, Mohajerani MH (2023) Hippocampal conjunctive and complementary CA1 populations relate sensory events to movement. iScience 26:106481.

Ji D, Wilson MA (2007) Coordinated memory replay in the visual cortex and hippocampus during sleep. Nat Neurosci 10:100–107.

Johnson A, Redish AD (2007) Neural ensembles in CA3 transiently encode paths forward of the animal at a decision point. J Neurosci 27:12176–12189.

Jung MW, Wiener SI, McNaughton BL (1994) Comparison of spatial firing characteristics of units in dorsal and ventral hippocampus of the rat. J Neurosci 14:7347.

Katche C, Dorman G, Slipczuk L, Cammarota M, Medina JH (2013) Functional integrity of the retrosplenial cortex is essential for rapid consolidation and recall of fear memory. Learn Mem 20:170–173.

Kentros CG, Agnihotri NT, Streater S, Hawkins RD, Kandel ER (2004) Increased attention to spatial context increases both place field stability and spatial memory. Neuron 42:283–295.

Kim SM, Ganguli S, Frank LM (2012) Spatial information outflow from the hippocampal circuit: distributed spatial coding and phase precession in the subiculum. J Neurosci 32:11539.

Knierim JJ, Kudrimoti HS, McNaughton BL (1995) Place cells, head direction cells, and the learning of landmark stability. J Neurosci 15:1648–1659.

Kudrimoti HS, Barnes CA, McNaughton BL (1999) Reactivation of hippocampal cell assemblies: effects of behavioral state, experience, and EEG dynamics. J Neurosci 19:4090–4101.

Lande AS, Garvert AC, Ebbesen NC, Jordbræk SV, Vervaeke K (2023) Representations of tactile object location in the retrosplenial cortex. Curr Biol 33:4599–4610.e7.

Lee I, Yoganarasimha D, Rao G, Knierim JJ (2004) Comparison of population coherence of place cells in hippocampal subfields CA1 and CA3. Nature 430:456–459.

Lein ES, et al. (2007) Genome-wide atlas of gene expression in the adult mouse brain. Nature 445:168–176.

Leutgeb S, Leutgeb JK, Barnes CA, Moser EI, McNaughton BL, Moser M-B (2005) Independent codes for spatial and episodic memory in hippocampal neuronal ensembles. Science 309:619–623.

Long X, Zhang S-J (2021) A novel somatosensory spatial navigation system outside the hippocampal formation. Cell Res 31:649–663.

Makino H, Komiyama T (2015) Learning enhances the relative impact of top-down processing in the visual cortex. Nat Neurosci 18:1116–1122.

Mao D, Kandler S, McNaughton BL, Bonin V (2017) Sparse orthogonal population representation of spatial context in the retrosplenial cortex. Nat Commun 8:243.

Mao D, Molina LA, Bonin V, McNaughton BL (2020) Vision and locomotion combine to drive path integration sequences in mouse retrosplenial cortex. Curr Biol 30:1680–1688.

Mao D, Neumann AR, Sun J, Bonin V, Mohajerani MH, McNaughton BL (2018) Hippocampus-dependent emergence of spatial sequence coding in retrosplenial cortex. Proc Natl Acad Sci U S A 115:8015–8018.

Marr D (1971) Simple memory: a theory for archicortex. Philos Trans R Soc Lond B Biol Sci 262:23–81.

McClelland JL, McNaughton BL, O'Reilly RC (1995) Why there are complementary learning systems in the hippocampus and neocortex: insights from the successes and failures of connectionist models of learning and memory. Psychol Rev 102:419–457.

Monaghan DT, Cotman CW (1985) Distribution of N-methyl-D-aspartate-sensitive L-[3H]glutamate-binding sites in rat brain. J Neurosci 5:2909–2919.

Moriyoshi K, Masu M, Ishii T, Shigemoto R, Mizuno N, Nakanishi S (1991) Molecular cloning and characterization of the rat NMDA receptor. Nature 354:31–37.

Nadel L, Willner J (1980) Context and conditioning: a place for space. Physiol Psychol 8:218–228.

Navratilova Z, Hoang LT, Schwindel CD, Tatsuno M, McNaughton BL (2012) Experience-dependent firing rate remapping generates directional selectivity in hippocampal place cells. Front Neural Circuits 6:6.

Neunuebel JP, Knierim JJ (2014) CA3 retrieves coherent representations from degraded input: direct evidence for CA3 pattern completion and dentate gyrus pattern separation. Neuron 81:416–427.

Okada S, Igata H, Sasaki T, Ikegaya Y (2017) Spatial representation of hippocampal place cells in a T-maze with an aversive stimulation. Front Neural Circuits 11:101.

O'Keefe J (1976) Place units in the hippocampus of the freely moving rat. Exp Neurol 51:78–109.

O'Keefe J, Dostrovsky J (1971) The hippocampus as a spatial map. Preliminary evidence from unit activity in the freely-moving rat. Brain Res 34:171–175.

Onodera K, Kato HK (2022) Translaminar recurrence from layer 5 suppresses superficial cortical layers. Nat Commun 13:2585.

Pachitariu M, Stringer C, Dipoppa M, Schröder S, Rossi LF, Dalgleish H, Carandini M, Harris K (2016) Suite2p: beyond 10,000 neurons with standard two-photon microscopy. BioRxiv, 061507.

Petersen CCH, Crochet S (2013) Synaptic computation and sensory processing in neocortical layer 2/3. Neuron 78:28–48.

Petreanu L, Mao T, Sternson S, Svoboda K (2009) The subcellular organization of neocortical excitatory connections. Nature 457:1142–1145. www.nature.com/nature.

Peyrache A, Khamassi M, Benchenane K, Wiener SI, Battaglia FP (2009) Replay of rule-learning related neural patterns in the prefrontal cortex during sleep. Nat Neurosci 12:919–926.

Pfeiffer BE, Foster DJ (2013) Hippocampal place-cell sequences depict future paths to remembered goals. Nature 497:74–79.

Pnevmatikakis EA, et al. (2016) Simultaneous denoising, deconvolution, and demixing of calcium imaging data. Neuron 89:285–299.

Qin YL, McNaughton BL, Skaggs WE, Barnes CA (1997) Memory reprocessing in corticocortical and hippocampocortical neuronal ensembles. Philos Trans R Soc Lond B Biol Sci 352:1525–1533.

Rao RPN, Ballard DH (1999) Predictive coding in the visual cortex: a functional interpretation of some extra-classical receptive-field effects. Nat Neurosci 2:79–87.

Richter D, Ekman M, de Lange FP (2018) Suppressed sensory response to predictable object stimuli throughout the ventral visual stream. J Neurosci 38:7452.

Rolls ET (2013) A quantitative theory of the functions of the hippocampal CA3 network in memory. Front Cell Neurosci 7:98.

Saleem AB, Diamanti EM, Fournier J, Harris KD, Carandini M (2018) Coherent encoding of subjective spatial position in visual cortex and hippocampus. Nature 562:124–127.

Sato M, et al. (2020) Distinct mechanisms of over-representation of landmarks and rewards in the hippocampus. Cell Rep 32:107864.

Schwindel CD, McNaughton BL (2011) Hippocampal–cortical interactions and the dynamics of memory trace reactivation. Prog Brain Res 193:163–177.

Sermet BS, Truschow P, Feyerabend M, Mayrhofer JM, Oram TB, Yizhar O, Staiger JF, Petersen CCH (2019) Pathway-, layer- and cell-type-specific thalamic input to mouse barrel cortex. eLife 8:e52665.

Skaggs WE, McNaughton BL (1996) Replay of neuronal firing sequences in rat hippocampus during sleep following spatial experience. Science 271:1870–1873.

Skaggs WE, McNaughton BL, Gothard KM, Markus EJ (1993) An information-theoretic approach to deciphering the hippocampal code. In:

Advances in neural information processing systems 5 (Hanson SJ, Cowan JD, Giles CL, eds), pp 1030–1037. San Mateo: Morgan Kaufmann.

Skoglund TS, Pascher R, Berthold CH (1997) The existence of a layer IV in the rat motor cortex. Cereb Cortex 7:178–180.

Smith DM, Barredo J, Mizumori SJY (2012) Complimentary roles of the hippocampus and retrosplenial cortex in behavioral context discrimination. Hippocampus 22:1121–1133.

Squire LR, Alvarez P (1995) Retrograde amnesia and memory consolidation: a neurobiological perspective. Curr Opin Neurobiol 5:169–177.

Srinivasan MV, Laughlin SB, Dubs A (1982) Predictive coding: a fresh view of inhibition in the retina. Proc R Soc Lond, B, Biol Sci 216:427–459.

Sugar J, Witter MP, van Strien NM, Cappaert NLM (2011) The retrosplenial cortex: intrinsic connectivity and connections with the (para)hippocampal region in the rat. An interactive connectome. Front Neuroinform 5:7.

Summerfield C, Trittschuh EH, Monti JM, Mesulam M-M, Egner T (2008) Neural repetition suppression reflects fulfilled perceptual expectations. Nat Neurosci 11:1004–1006.

Sun Y, et al. (2019) CA1-projecting subiculum neurons facilitate object–place learning. Nat Neurosci 22:1857–1870.

Takehara-Nishiuchi K, McNaughton BL (2008) Spontaneous changes of neocortical code for associative memory during consolidation. Science 322:960–963.

Teyler TJ, DiScenna P (1986) The hippocampal memory indexing theory. Behav Neurosci 100:147–154.

Todd TP, Mehlman ML, Keene CS, DeAngeli NE, Bucci DJ (2016) Retrosplenial cortex is required for the retrieval of remote memory for auditory cues. Learn Mem 23:278–288.

Todorovic A, van Ede F, Maris E, de Lange FP (2011) Prior expectation mediates neural adaptation to repeated sounds in the auditory cortex: an MEG study. J Neurosci 31:9118.

Treves A, Rolls ET (1994) Computational analysis of the role of the hippocampus in memory. Hippocampus 4:374–391.

Ueta Y, Otsuka T, Morishima M, Ushimaru M, Kawaguchi Y (2014) Multiple layer 5 pyramidal cell subtypes relay cortical feedback from secondary to primary motor areas in rats. Cereb Cortex 24:2362–2376.

van Groen T, Wyss JM (1992) Connections of the retrosplenial dysgranular cortex in the rat. J Comp Neurol 315:200–216.

van Groen T, Wyss JM (2003) Connections of the retrosplenial granular b cortex in the rat. J Comp Neurol 463:249–263.

Vedder LC, Miller AMP, Harrison MB, Smith DM (2017) Retrosplenial cortical neurons encode navigational cues, trajectories and reward locations during goal directed navigation. Cereb Cortex 27:3713–3723.

Vogt BA, Miller MW (1983) Cortical connections between rat cingulate cortex and visual, motor, and postsubicular cortices. J Comp Neurol 216:192–210.

Wilson MA, McNaughton BL (1993) Dynamics of the hippocampal ensemble code for space. Science 261:1055–1058.

Wilson MA, McNaughton BL (1994) Reactivation of hippocampal ensemble memories during sleep. Science 265:676–679.

Yamawaki N, Borges K, Suter BA, Harris KD, Shepherd GMG (2014) A genuine layer 4 in motor cortex with prototypical synaptic circuit connectivity. eLife 3:e05422.

Yamawaki N, Radulovic J, Shepherd GMG (2016) A corticocortical circuit directly links retrosplenial cortex to M2 in the mouse. J Neurosci 36:9365.

Yong HC, Chang H, Brandon MP (2022) Optogenetic reduction of theta oscillations reveals that a single reliable time cell sequence is not required for working memory. BioRxiv, 2022.06.25.497592.

Zhang K, Ginzburg I, McNaughton BL, Sejnowski TJ (1998) Interpreting neuronal population activity by reconstruction: unified framework with application to hippocampal place cells. J Neurophysiol 79:1017–1044.

Zielinski MC, Shin JD, Jadhav SP (2019) Coherent coding of spatial position mediated by theta oscillations in the hippocampus and prefrontal cortex. J Neurosci 39:4550–4565.

Ziv Y, Burns LD, Cocker ED, Hamel EO, Ghosh KK, Kitch LJ, El Gamal A, Schnitzer MJ (2013) Long-term dynamics of CA1 hippocampal place codes. Nat Neurosci 16:264–266.